2004

Assessment of shearing phenomenon and porosity of porous media using microfocus computed tomography

Bashar Adeeb Alramahi
Louisiana State University and Agricultural and Mechanical College, balram1@lsu.edu

ASSESSMENT OF SHEARING PHENOMENON AND POROSITY OF POROUS MEDIA USING MICROFOCUS COMPUTED TOMOGRAPHY

A Thesis

Submitted to the Graduate School of the
Louisiana State University and
Agricultural and Mechanical College
in partial fulfillment of the
requirements for the degree of
Master of Science in Civil Engineering

in

The Department of Civil and Environmental Engineering

By
Bashar A. Alramahi
B.Sc. Birzeit University, Ramallah, Palestine 2002
August, 2004

DEDICATION

To the memory of my father

To my mother and brother

&

To my family and friends

ACKNOWLEDGMENTS

First, I would like to express my deepest thanks to my family. I am really grateful for all the love and support they always provided.

I would like to acknowledge the efforts of my advisor Dr. Khalid Alshibli. The help and guidance he provided for me throughout my graduate study at Louisiana State University are deeply appreciated. I would like to extend my thanks to the members of my committee, Dr. Dante Fratta and Dr. Emir Macari. I am grateful of all the help and support they always provided.

I would like to thank my dear friends, Dr. Mustafa Alsaleh, Sacit, Victor, Lynne, Heath, Rich, Brenda and Munir for all the great times we spent together. I would also like to acknowledge the contribution of Patrik Furlong, Irshad Syed and Vida Sharafkhani from Louisiana State University for help in the data collection.

Special thanks are due to Dr. Ron Beshears and Mr. David Myers of NASA/ Marshall Space Flight center for helping us to perform the CT scans of the plastic beads. I thank Professor Balasingam Muhunthan, director of WAX-CT Laboratory and Mohammad Reza Razavi, Graduate student of Washington State University for allowing us to perform the CT scans of the rock cores, I also thank Mr. David Philips of HYTEC Inc. for providing the FlashCT_VIZ software.

This research is partially funded by the Louisiana Transportation Research Center (LTRC Project No. 02-07GT) and the Louisiana Department of Transportation and Development (State Project No. 736-99-1057) through Transportation Innovation for Research Exploration (TIRE) program.

TABLE OF CONTENTS

ABSTRACT

Microfocus x-ray computed tomography (μCT) is a powerful non-destructive scanning technique to study the internal fabric of granular materials. In this thesis, μCT was applied to two cases. The first case involves studying the behavior of particles in a triaxial specimen during shearing. Three-dimensional translation and rotation of the particles were tracked throughout the shearing process, and they were used to calculate the local strain distributions including the axial, radial, and rotation strains. Moreover, the local dilatancy angle distribution was calculated for all the different levels of the experiment. These distributions were compared to study the changes in the behavior of the particles at different stages of the test. Furthermore, 3D renderings and animations showing the particles behavior throughout the test were generated.

It was noticed that the radial strains ε_x and ε_y showed a similarity throughout the test due to the axisymmetric conditions of the test. It was also found that high rotation angles took place, where the vertical rotation component reached up to 30 degrees and the horizontal rotation reached up to 60 degrees. Furthermore, the rotation strain component reached up to about 50% at the end of the test. On the other hand, a wide range of local dilatancy angles was observed, where the values varied between -50 degrees and 70 degrees, and the fraction of the positive values (dilation) increased as the test proceeds.

The second part of this thesis aims at determining the effect of grain size distribution and consolidation pressure on the spatial porosity distribution of synthetic rock cores. Twelve rock cores were prepared with different grain size distributions and consolidation pressures, and scanned using a high resolution μCT system. Density calibration was conducted to correlate the CT numbers to the bulk density, and the

porosity of the cores. A computer algorithm was developed to calculate the local porosity values, producing about 15 million values per core. μCT showed an excellent ability to track the changes in the local porosity distribution of the cores. It was found that grain size distribution has a larger effect on the porosity values, where a noticeable decrease in the porosity values was observed when using well graded grains. On the other hand, increasing the consolidation pressure did not always decrease the porosity values. This could be due to the crushing of the particles at very high consolidation pressures.

CHAPTER ONE

INTRODUCTION

1.1 BACKGROUND

To study the mechanical behavior of granular materials, many factors should be considered, like the particles' arrangement, particle groups' association, packing density, particle shapes, and the inter-particle configuration. The analysis techniques for these factors are usually classified as destructive and non destructive. Destructive techniques include specimen stabilization and thin sectioning, while the nondestructive techniques include magnetic resonance imaging, ultrasonic testing, x-ray radiography and x-ray computed tomography (Alshibli et al., 2000a).

Computed tomography is an imaging technique in which an object is placed between an x-ray source and a detector, and the object is rotated while the x-ray passes through it collecting information about its internal structure. The information is reconstructed to create a two-dimensional cross section "slice" of the object that can be used to view the internal structure of the object (Cromwell, 1984). Slices can also be stacked together to create a three dimensional volume view of the scanned object. Alshibli et. al (2000a) showed that CT is able to detect specimens' inhomogeneities, localization patterns, and quantify void ratio variation within sand specimens.

Many numerical and experimental efforts have been made to understand and predict the behavior of granular materials during shearing. Many assumptions had been made to describe the sliding and rolling of the particles during shearing. The non-destructive visualization abilities provided by CT makes it possible to achieve a better understanding of the particles' interaction during shearing at the microscopic level. This will help to improve the modeling of the

constitutive behavior of granular materials. It also could be used to validate the previous assumptions about the particles' behavior.

Investigating the spatial distribution of porosity in rock cores is of great importance in petroleum engineering and ground water hydrology. Recent advances in computed tomography have increased the potential of conducting an accurate assessment of porosity distribution within rock cores and linking such measurements to other physical properties such as permeability and pore space distribution. CT is a very effective tool to study this property. It has the ability to detect the effects of small change in particle size distribution and compaction pressure of rock cores on their porosity distribution. The results of this research might result in improving current models that link porosity of rocks to their permeability and tortuosity..

1.2 OBJECTIVES

The main objective of this thesis is to apply microfocus computed tomography to study micro-properties of geomaterials. Two cases will be studied; they are:

I) Study the shearing of granular materials: a triaxial specimen was scanned at different strain levels to track the translation and rotation of the particles within the specimen. The obtained values for translation and rotation will be used to calculate the local strain distribution within the specimen. And the distributions will be compared to study the behavior of the particles at different stages of the experiment. Also, three dimensional renderings and animations will be generated in order to show the particle movement and rotation throughout the experiment.

II) Characterize the variation of the local porosity of rock cores: assess spatial porosity distribution of synthetic rock cores, and the effect of using different compaction pressures and different grain size distributions on these values.

1.3 THESIS OUTLINE

Chapter 2 of this thesis will present a literature review about x-ray computed tomography, including a description of the scanning process, the engineering applications, the development of CT scanners, and artifacts in CT images. It also presents some of the previous efforts in the field of studying the behavior of granular materials during shearing and porosity measurements.

A description of the experimental work conducted in order to achieve the first objective, including the materials used, specimen preparation and the scanning process is presented in Chapter 3. It also includes the methods used to view the CT images and data collection. Chapter 4 includes a presentation of the results of this study, along with the analysis and discussion of these results.

The experimental work conducted in order to achieve the second objective, a description of the rock cores and the CT scanning process, and the results of the study are presented in Chapter 5. The conclusion of this thesis along with the remarks and recommendations for future work are presented in Chapter 6.

CHAPTER TWO

LITERATURE REVIEW

2.1 X-RAY COMPUTED TOMOGRAPHY

2.1.1 History

X-ray was originally discovered by the German physicist Wilhelm Konrad Rontgen in 1895, for that he was awarded the Nobel Prize in physics in 1901. Since then, X-ray radiography was widely used in the medical field to view and diagnose internal body organs (KTH, 2001).

Applications of radiography extended from the medical field to industrial applications as a very useful non destructive tool to investigate the internal structure of the bodies. But the capabilities of radiography were limited to providing a 2D projection of the internal structure of a body, which could not provide enough details (Sheats, 2000).

In 1971 Godfrey Hounsfield of England's EMI laboratories developed the technology known as Computed tomography, in which detailed internal structural information about the body could be obtained (Barrington, 2004).

2.1.2 Radiography versus CT

A neutron or x-ray source and a piece of film are used in radiography. When the radiation passes through an object it is attenuated, and a projection of the internal structure is created when the x-ray reaches the film (Sheats, 2000). Therefore, the three dimensional (3D) structure of the body is represented by a 2D projection, and the depth dimensions are lost where all the planes perpendicular to the direction of the x-ray are superimposed over each other.

On the other hand CT could overcome this problem by producing a 2D image of the plane (called slice) through the object then the images of all the different planes are stacked on top of each other to create a 3D volume. In CT the measurements are made on a narrow fan beam of x-rays through the slice from many different directions and an image is reconstructed mathematically from these measurements through a large number of line integrals. The depth information here could be obtained by scanning the slice from many different directions to be considered in the reconstruction process of the slice (Michael, 2001). Figure 2.1 shows a schematic of the CT and Radiography processes.

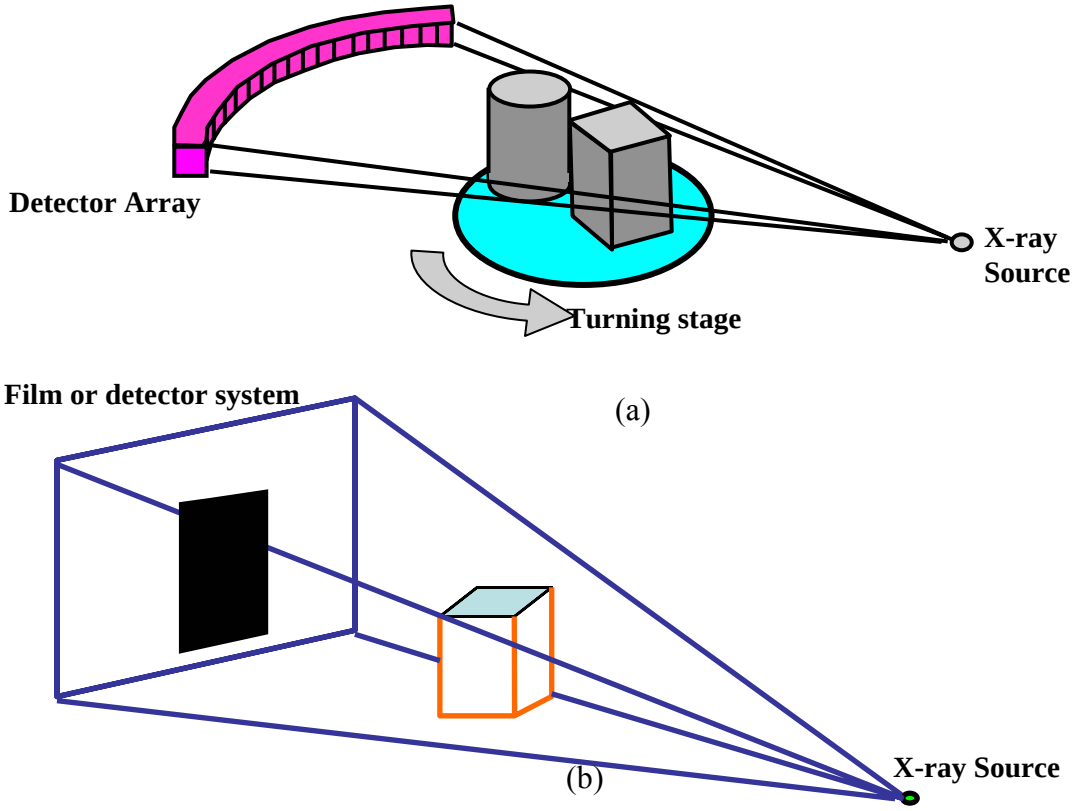

Figure 2.1. Schematics of (a) CT system (b) Radiography system

A further improvement to CT imaging was achieved by implementing the microfocus X-ray sources in the computed tomography facilities. This was known as “Microfocus Computed

Tomography μCT". This technology uses a new type of X-ray tube whose X-ray focus is from a fraction of a micron to 10 μm. It mainly has an acceleration voltage from 100 kV to 225 kV. Using this tube largely magnified the projection data of the object without degradation of the sharpness obtained (Fujii, 2003). Using μCT enhanced the resolution of the systems to the order of (10μm x 10 μm x 10 μm) for small objects instead of (60 μm x 60 μm x 1 mm) obtained by the conventional CT systems (Wevers et al., 2000). Moreover, it can be realized that using μCT, the same high resolution could be obtained in the z-direction, reducing the thickness of the slice, and improving the CT image quality.

2.1.3 The Interaction of x-ray with Matter and CT Number

When the x-ray passes through matter, the photons are either scattered with some loss of energy, or completely absorbed in a photoelectric interaction, as a result, some photons will be lost from the beam while passing through matter. Only part of the photons will remain in the beam and reach to the detector, which means that a beam of photons is not degraded in energy as a result of passing through matter, just attenuated in intensity (KTH, 2001).

The probability of photon attenuation can be expressed per thickness of the attenuator, with the Beer equation:

$$I(x) = I_0 e^{-\mu x} \quad \ldots\ldots (2.1)$$

Where I is the x-ray intensity at certain distance x, I_0 is the x-ray intensity when it is emitted from the source, and μ is the linear attenuation coefficient which can be defined as the probability that an x-ray or gamma-ray photon will interact with the material it is traversing per unit path length traveled. It is usually reported in cm^{-1}. The linear attenuation coefficient depends on the photon energy, the chemical composition and physical density of the material (Amersham Health, 2003). Usually, the dependency of the linear attenuation on the density of the material is

overcome by normalizing it to the density. The normalized value of the linear attenuation is called the mass attenuation (μ/ρ). The mass attenuation for any material can be calculated as the weighted average of the mass attenuations of the component elements, where the mass attenuation of each element is multiplied by its fracture by weight of the composite (Amersham Health, 2003).

The obtained CT numbers in a CT scan are directly proportional to the local electron density of the material under investigation (Bossi el al. 1990). The CT scanner measures density as a CT number (Alfaro et al. 2001), which is defined as (Otani et al. 2000):

$$CTN = \frac{(\mu_t - \mu_w)\kappa}{\mu_w} \quad \ldots\ldots\ldots\ldots\ldots\ldots\ldots\ldots\ldots\ldots\ldots\ldots\ldots\ldots \quad (2.2)$$

Where μ_t is the linear attenuation of the material and μ_w is the linear attenuation of water, and κ is a scaling factor either 500 or 1000 (Alfaro, 2001). However, different CT scanners generate different CT number ranges (κ) depending on their reconstruction algorithms.

If a pixel (or a voxel which is a three dimensional pixel) lies in more than one material the CT number for this pixel is calculated as the weighted average of the CT numbers of the different materials considering the percentage of the volume occupied by the material from the total voxel volume.

The standard mass attenuation coefficients (μ/ρ) can be obtained for different materials from The National Institute of Standards and Technology (NIST) website, and the mass attenuation of composite materials can always be calculated as the sum of the mass attenuation of each material in the mixture multiplied by its fraction weight (w_i). i.e;

$$\mu / \rho = \sum_i w_i (\mu / \rho)_i \quad \ldots\ldots\ldots\ldots\ldots\ldots\ldots\ldots\ldots\ldots\ldots\ldots\ldots\ldots\ldots\ldots\ldots\ldots \quad (2.3)$$

This also applies to dry or saturated soil samples where the mass attenuation is calculated considering the mass attenuations of the soil and water (or air) and their fraction by weight.

Depending on the value of the CT number, pixels take different color intensities between black and white (gray scale). This scale is set in 256 grey levels, starting from black for low CT values and ending in white for high CT values. In other words, light materials (like air) appear in the CT image as black or dark grey pixels, and denser materials (like soil minerals) have a lighter color, getting closer to the white color as density increases. A sample slice image obtained by CT is shown in Figure 2.2. Stacking slices together results in creating a volumetric view of the scanned object. A sample volume view is shown in Figure 2.3.

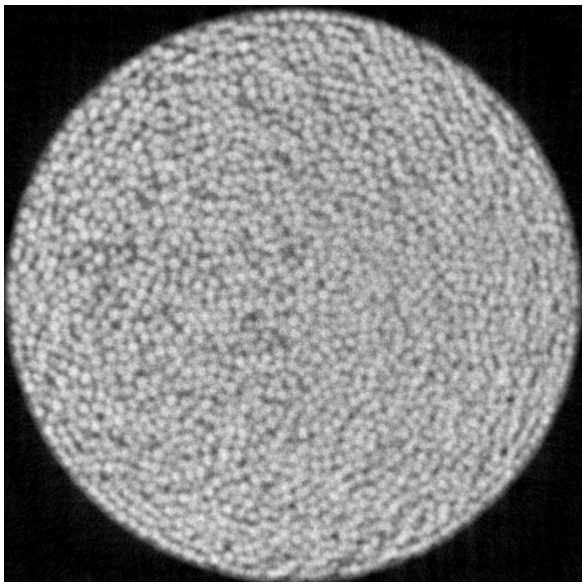

Figure 2.2. A sample CT slice (Alshibli, 2004)

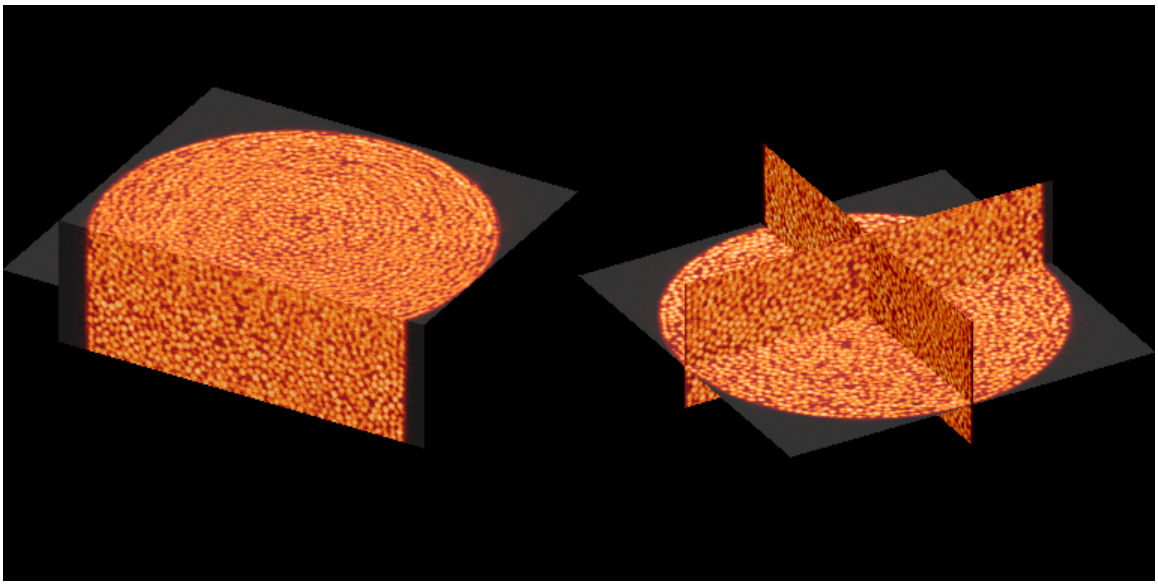

Figure 2.3. Visualization of the volume (Alshibli, 2004)

2.1.4 Applications of Microfocus Computed Tomography

μCT was first used in diagnostic medical fields to acquire 3D images of the internal body organs and tissues. First it was used to scan the human head, and then it was used all over the body. In the field of materials research, it was widely used in petroleum engineering for core analysis, μCT images were used for characterization of reservoir rocks, for mineral formation and rock property evaluation (e.g. Honarpour et al. 1985). It was also used for monitoring two and three-phase experiments in porous media (e.g. Bansal et al. 1991) and to verify and analyze the multiphase fluid flow in porous media (e.g. Cromwell et al. 1984). In the field of geotechnical engineering, μCT was used to observe localized deformations and shear bands in specimens undergoing triaxial compression, void ratio evolution inside shear bands, void ratio variation in soil specimens, and characterization of failure in soils. (Desrues et al. 1996, Otani et al. 2000, Alshibli et al. 2000a,b). Figure 2.4 shows an example of using μCT images to view the deformation of a specimen undergoing a triaxial compression test.

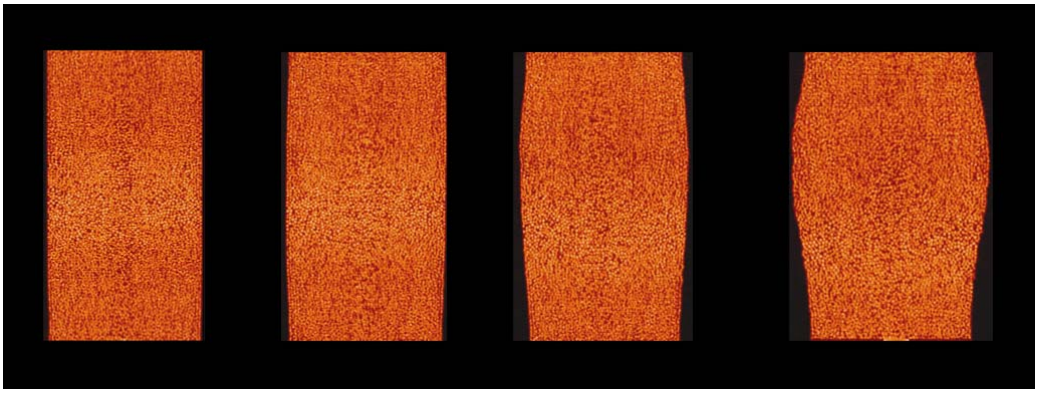

Figure 2.4. The deformation of a specimen in a triaxial test (Alshibli, 2004)

2.1.5 The Development of CT Scanners

The majority of the CT scanners in use are classified to five generations, which mainly differ in mechanical configuration of the equipment, the relative motion of the scanned object, the x-ray source, the detectors, and the amount of the x-ray energy (Figure 2.5). The type of the scanner will influence the CT image quality, and scanning times, therefore, a tradeoff between the scanning time and quality (resolution) of the images must take place. For example in the medical field the patient is required to remain motionless until the scanning process is finished, therefore, time is a very important factor in medical CT. Moreover, the amount of energy to be used must be low to be tolerated by the human body. On the other hand, in industrial CT time is a less important factor and better quality images could be obtained utilizing the availability of a greater scanning time. Higher energies could be used without affecting the scanned object. (Kropas-Hughes et al. 2000)

First generation CT scanners use a single x-ray source and a single detector, this geometry is called: Parallel Beam Geometry. Multiple measurements of the x-ray transmission are obtained using a single highly collimated x-ray pencil beam and detector (Yoshikawa, 2004). The x-ray source and detector are translated along the scanned object to obtain a single view, and

then they are rotated to obtain another view. Then all the views are collected to build a slice. This is called a “Translation-Rotation” motion which yields good quality images but it needs a very long time to perform.

Second generation CT scanners use the same “Translation-Rotation” motion but instead of having a single x-ray beams, a fan beam of radiation and a linear array of detectors are used. This enables the scanner to obtain multiple views of the object within a single translation, resulting in reducing the scanning time by about 10 times for each slice (Kropas-Hughes et al. 2000).

In third generation CT scanner, a curved detector array containing a large number of detectors is used with the x-ray source to obtain a complete view of the object without translation. Multiple views are obtained by the rotation of the source and the detector arrays around the object. This is called a “Rotate only” motion, and it reduces the scanning time to a small fraction of the time needed by the first two generations. In this type of scanners, the quality (resolution) of the obtained images, depend mainly on the number and size of the sensors in the detector. Therefore, a very large number of sensors has to be used in order to get an acceptable quality for the images, but it is still hard to get the same quality for the image as in the first and second generation systems (Kropas-Hughes et al. 2000).

Fourth generation CT scanners also use the “Rotate only” motion, but it is different from the third generation since it uses a stationary circular array of detectors. The source rotates around the body shooting a wide fan beam of x-ray. A view is made by obtaining successive absorption measurements of a single detector at successive positions of the x-ray source. These scanners are faster and have a better artifacts resistance than the other CT scanners, but they are more susceptible to scattered radiation (Yoshikawa, 2004).

Fifth generation CT scanners are different than all the other scanners since no motion is involved. In this scanner, a circular array of x-ray sources, which are electronically turned on and off is used. The detectors in this scanner are substituted by a large florescent screen so that when an x-ray source is switched on, a large volume of the object is imaged simultaneously. This scanner acquires two dimensional projections of three dimensional objects rather than the one dimensional projections of two dimensional objects. The projection data can be acquired in approximately 50 ms (Yoshikawa, 2004), which is fast enough the image the moving parts like a beating heart, therefore, this scanner is used mostly in the medical field rather than the industrial applications.

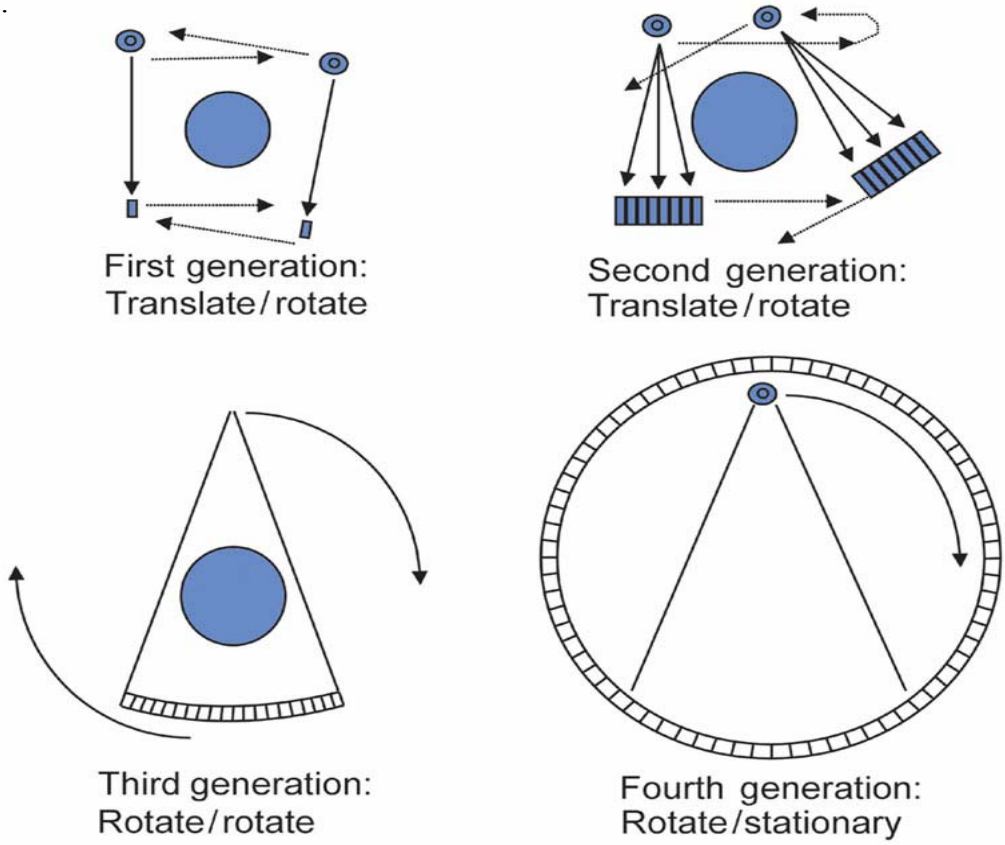

Figure 2.5. (a) First generation single pencil beam translate/rotate scanner; (b) second generation multiple pencil beam translate/rotate scanner; (c) third generation rotate/rotate fan beam scanner; (d) fourth generation rotate/stationary inverted fan beam scanner. (Amersham Health, 2004)

2.1.6 Artifacts in CT

An artifact can be defined as any information in the CT image that does not reflect the actual composition of the scanned object. Many types of artifacts are encountered during a CT scan. Artifacts in a CT image can be originated by many factors like the characteristics of the scanned object including its shape and chemical composition, the x-ray nature, the detectors quality, and the resolution of the system.

Beam hardening or cupping is one of the most commonly encountered artifacts (Mukunoki et al., 2003), it takes place when a polychromatic X-ray (which is an x-ray whose spectrum contains photons with different energies) loses its lower energy photons while passing through matter due to attenuation. As a result, the average energy of the beam is increasing, in other words, it is hardening. Since it is harder to attenuate higher energy beams, as the beam travels deeper in the material, less attenuation takes place, resulting in lower CT numbers, consequently the image gets darker as the center of the object is approached, giving a false implication of a lower density of the material. This artifact can be reduced by increasing the x-ray energy from the source, or adding a metallic filter in front of the source that reduces the amount of lower energy photons. Ketcham et al. (2001) stated that an x-ray beam with higher energy propagates more effectively than with lower energy, but it is less sensitive to changes in material density and composition. Therefore, as an alternative solution, a mathematical correction in the reconstruction process can be used (Wevers et al. 2000).

Partial volume effect is another type of artifacts which is mainly affected by the spatial resolution of the CT scan. The CT number of a voxel represents the attenuation properties of the material where the voxel lies. When two or more materials lie in the area of the voxel (e.g. air and soil) the CT value of the voxel represents the average of the values of the different materials,

and the true structure of soil particles will not be represented (Mukunoki et al., 2003). This problem mainly appears when very small particle sizes are used in the CT scan, increasing the possibility of having more than one material within a voxel. Increasing the resolution of the system, in other words, reducing the size of the voxel will reduce the possibility of the partial volume artifacts, and the internal structure would be represented more accurately. It should be noted that increasing the spatial resolution will significantly increase the scanning time, and the size of the data sets, therefore, a trade off between these factors has to be considered.

Some other artifacts are also encountered, like the ones caused by the motion of the scanned object, which produces the greatest degree of artifacts in the medical field (Strumas et al. 1995). Also, there is the star or streak artifact which is caused by the secondary radiation that augments the noise and creates the artifact (Wevers et al. 2000). Another cause of the streak artifact is the presence of a highly attenuating piece of metal that attenuates all or a part of the x-ray causing the attenuation measurement to be incorrect.

2.2 APPLICATIONS OF CT TO STUDY POROSITY AND FABRIC OF POROUS MEDIA

2.2.1 Density Calibration of CT Data

The CT image data can be used to perform material density measurements. ASTM-E1935, 97 specifies a standard method to perform a CT density calibration and measurement, in which several materials of known mass attenuations and bulk densities are scanned at the same energy as the scanned object. Then the mean CT number is measured for each material and a correlation between the CT number and the linear attenuation of the material is obtained, where the linear attenuation equals the mass attenuation multiplied by the bulk density of the material. The next step is to measure the mean CT number in a specified area of the scanned object (soil specimen for example), and applying the correlation obtained above, the linear attenuation of the

material is calculated. The bulk density of the object will be then equal to the linear attenuation divided by the mass attenuation.

This technique is helpful in studying geomaterials mainly because the bulk density can be used to calculate the void ratio (e) or porosity (n) of the material, which are two important parameters used in assessing the material properties. The equations used to calculate porosity (n) are as follows:

For a saturated material:

$$n = \frac{G_s - \frac{\rho_{sat}}{\rho_w}}{G_s - 1} \quad \text{..... (2.4)}$$

For a dry material:

$$n = 1 - \frac{\rho_d}{\rho_w G_s} \quad \text{..... (2.5)}$$

And in general:

$$n = 1 - \frac{\frac{\rho}{\rho_w}}{G_s(1+w)} \quad \text{..... (2.6)}$$

Where G_s is the specific gravity of the material, ρ is the bulk density, and *w* is the water content.

2.2.2 Using CT for Porosity Measurements

Porosity (or voids ratio) of rocks is an important physical property since it provides key answers about the distribution of fluids or oil within rock strata. It depends on many factors including grain size distribution, grain shape, rock formation history, cementation and overburden (consolidation) pressure. CT was used to study the porosity of rock cores by many researchers in the field of petroleum engineering. Withjack (1987) used CT for flow visualization

and determination of porosity of rock cores. He stated that average porosities determined by CT scanning of Berea and dolomite samples compare well (within $\pm 1\%$) of those determined conventionally. More recently Van Geet et al. (2003) discussed the potential and limitations of microfocus CT in quantifying porosity distribution of sedimentary rocks. They compared CT results with porosity measurements by other techniques like image analysis of thin sections, mercury porosimetry, and vacuum saturation.

Image analysis was used by Frost el al. (2000) to study the local void ratio distributions of sand specimen during triaxial tests. They stated that using a single value global void ratio may lead to masking of conditions that only exist in part of the specimen, but control the actual response of the complete specimen. At different levels of the experiments, the specimens were impregnated with epoxy resin, then horizontal and vertical coupons are cut, and the surfaces were polished. Optical microscope pictures were acquired at various locations of the surfaces. Void ratios were calculated as the ratios of the areas of solids to voids in a 5 mm by 5 mm areas in the images. This technique yields good results for the void ratio distribution, but there are some shortcomings to this procedure. The long working hours required for polishing and slicing the specimen and the destructive nature of this approach (Van Geet et al 2003) makes it sometimes difficult to implement. Moreover, the void ratio measurement are conducted only on 13 to 15 areas in each slice, and then the void ratio values are interpolated for the rest of the areas in volume, where continuous measurements for the whole volume could be obtained using other techniques like x-ray computed tomography.

Computed tomography was used by many researchers to study the porosity or void ratio distributions of granular materials during shear. Desrues et al. (1996) used CT to study the local void ratio evolution in the shear bands of sand specimen during triaxial testing. Moreover,

Alshibli et al. (2000) used CT to quantify the void ratio variation of sands during triaxial tests conducted at very low confining stresses in a microgravity environment abroad a Space Shuttle during the NASA STS-79 and STS-89 missions. Contour maps and histograms of the void ratio of the specimen at different strain levels were produced.

2.2.3 The Behavior of Granular Particles during Shearing

Many attempts have been made by various researchers to understand, and be able to predict, the interaction of particles at the microscopic level during shearing. Oda et al. (1997) stated that particles' orientation changes sharply at shear band boundaries, therefore, a high gradient of particle rotation can be developed within a relatively narrow zone during the shear banding process. Moreover, while studying the localization phenomenon in granular materials using the micro-polar theory Vardoulakis et al. (1995) related the grain rotation to the average spin of a representative grain assembly which contains the grain. Kuhn et al. (2002) stated that particle rotations are known to have an important influence on the mechanical behavior of granular materials. They also listed some previous experimental efforts to understand the effect of micro-scale particle rotations.

Oda et al. (1999) reported that while a variety of successful testing apparatuses have been developed to study the stress strain behavior of granular media under a general stress state, little progress has been achieved in the technology of visualizing the micro-structure developed during deformation. Many studies have been conducted on ideal packings of spheres and were used to predict the general characteristics of granular materials.

Experimental efforts have been conducted to clearly understand the behavior of granular material during shearing. For example, Rowe (1962) conducted some experiments on ideal assemblies of rods in a parallel stack and spheres in cubic and rhombic packing. He applied a

deviatoric stress to the stack and measured the deformations by means of "micrometer and dial gauge". He observed the behavior of the particles during the different stages of compression, and tracked the changes in the contact angles between the particles. This effort led to the development of the well known "Rowe's stress-dilatancy theory".

Oda et al. (1982), carried out biaxial compression tests on assemblies of photo-elastically sensitive rod-like particles with oval cross sections in an effort to determine if particle rolling is important as a micro-mechanism of deformation. Also, tests were carried out using two-dimensional assemblies of circular wooden rods. A formation of rods in the central part of the assembly was pictured at each deformation step, and comparing the pictures at each step, the translation and rotation of the particles was calculated (Oda et al.1999).

Numerical models have been used to simulate the behavior of granular materials under stresses. For example, Kanatani (1979) suggested a micropolar continuum theory to describe the flow of granular materials. More recently, Anandarajah (2004) stated that Rowe's equations were solely based on interparticle sliding, and ignored interparticle rolling. Moreover, he criticized Rowe's equations that they ignore the hardening/softening exhibited by the soil, and that granular materials obey these equations for some initial densities, they disobey them for other initial densities. On the other hand, Anandarajah (2004) suggested a microstrucural model based on a combination of interparticle sliding and rolling to represent the constitutive behavior of a two dimensional assembly of granular particles. This was a purely mathematical model, and Anandarajah stated that no quantitative comparison between the theoretical results of his model and experimental results was sought.

CHAPTER THREE

PARTICLES BEHAVIOR DURING SHEARING OF GRANULAR MATERIALS

3.1 INTRODUCTION

The CT technology was used in this part of the research to study the behavior of granular materials while being sheared. An axisymmetric triaxial test was conducted on a cylindrical specimen and CT scans were acquired at different stages of the shearing process. Individual particles could be observed using the high quality images obtained, and tracked throughout the experiment. The data obtained by tracking individual particles can be used to calculate the amount of translation, sliding and rotation that every particle undergoes throughout the shearing process. The data can also be used to calculate the local strain values, and distributions, and the changes they undergo throughout the experiment.

This Chapter illustrates the experimental work that was conducted to achieve this study, including the description of the materials, preparation of the specimen, and a description of the CT scans. It also illustrates how the data was collected from the CT images. And finally, this Chapter includes the formulas used to calculate the translations, rotations, and local strains. The following Chapter will include a demonstration of the data obtained, and the results of the translation, rotation, and local strains calculations. It also includes a discussion of the results.

3.2 EXPERIMENTAL WORK

To be able to accurately track the movement of the particles, one must have a reference for each particle to be able to track its position and orientation as shearing proceeds. For this reason, plastic beads with holes was used in this study. The holes will serve as a reference for comparison of the positions and orientations of the beads in different scans.

Spherical plastic beads (Pearls) with a diameter of about 6.5 mm (Figure 3.1) were used to prepare the specimen. To further increase the visibility of the air holes, Aluminum wires were inserted through the holes of some beads. About 35 beads with wires were placed in three layers during the preparation of the specimen. Aluminum can be clearly identified in the scans since it has a different attenuation coefficient.

Figure 3.1. Spherical beads (SB)

The CT scans were conducted in October 2003 at NASA/ Marshall Space Flight Center (MSFC) CT facility in Huntsville, Alabama. The MSFC CT scanner is a third generation system called FlashCT manufactured by HYTEC Inc., Los Alamos, New Mexico. It incorporates an amorphous Silicone (a-Si) flat panel detector (Figure 3.2) that can accommodate objects with a projected area up to 304.8 mm x 406.4 mm (12 x 16 in). Second generation industrial CT systems use a line-detector array and therefore can only scan a thin slice (~1 mm thick) along the object axis. Then, the object is moved vertically to scan the next slice until the entire objected is covered. The flat-panel detector technology of the FlashCT system eliminates the need for time-consuming individual line scans associated with other types of industrial CT systems. It utilizes the concept of "volume tomography" where the entire specimen area is projected onto the CT

detector and the x-rays attenuation is collected simultaneously. Then the specimen is rotated to acquire the data for the next area. This reduces the scanning time by a factor of 100. The x-ray source of MSFC CT is Model No. MXRI-TC-450PS (Figure 3.3), manufactured by Marietta x-ray incorporated, Marietta, Georgia. It can generate x-rays with energy level up to 450 keV.

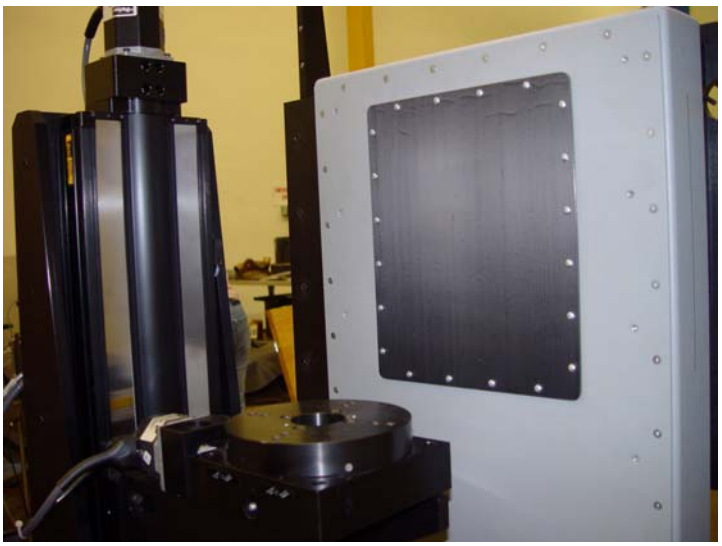

Figure 3.2: Detector panel and the stage of MSFC CT scanning system

Figure 3.3: The x-ray source of the MSFC CT system

A cylindrical specimen was prepared using the plastic beads (Figure 3.4). The specimen was held under constant vacuum confinement of 25 kPa. Since the objective of this study is to study particles' interaction, only the middle portion of the specimen was scanned. The Specimen was labeled with two small Aluminum plates that were attached to the membrane surface. They serve as spatial references for the CT images. The scanning window was kept constant for all scans performed on the specimen. Before each scan, a 12.7 mm (1/2 in) acrylic rod was attached to the specimen. It helps to calibrate the density of the specimen for various scans since the CT reconstruction software tends to change the CT number from one scan volume to another. Four CT scans were performed on the specimen at different strain levels. First, the specimen was scanned before compression (ε_z = 0%) using 100 keV energy at 1.8 mA current. Then, the acrylic rod was removed, the test cell was assembled and the specimen was compressed using the GeoJac loading system (Figure 3.5). The loading was then paused, and the CT scanning was performed. The process was repeated for the following two scans. It took approximately 10 minutes to scan the volume between the two Aluminum plates for each case. Post scan data processing took approximately 5 hours/scan producing about 570 slices per scan. Table 3.1 shows the initial dimensions of the specimen and the axial strain level at each CT scan, and Figure 3.6 shows the location of each CT scan on the stress-strain curve. Figure 3.7 shows the axial strain versus volumetric strain for the specimen. Load oscillations can be seen in both figures 3.6 and 3.7, this is due to a slip-stick mechanism that takes place when shearing this type of particles.

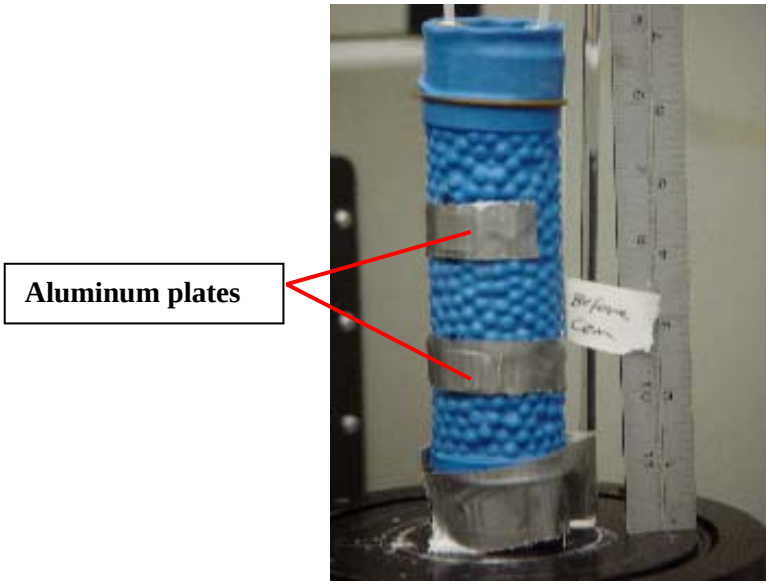

Figure 3.4. The specimen before compression

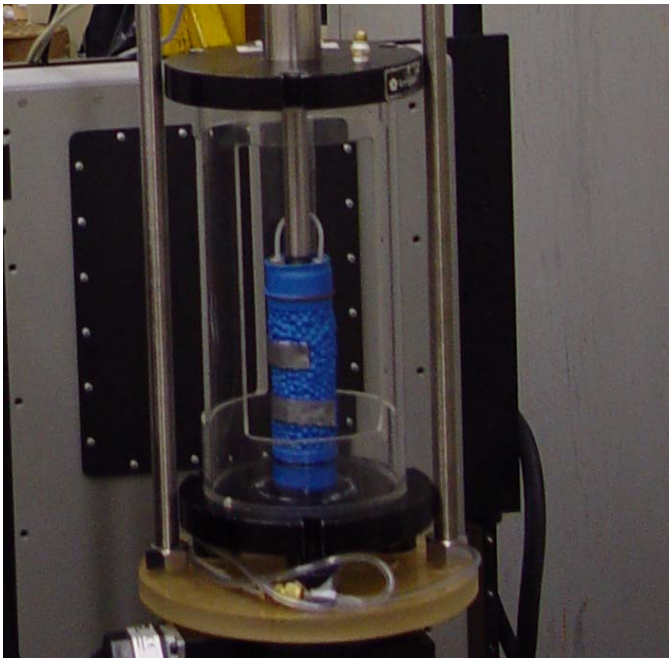

Figure 3.5. The specimen in preparation for compression on the stage of CT scanner

Table 3.1. Initial dimentions and strain values at every CT Scan

Specimen	Initial Diameter (mm)	Initial Height (mm)	First scan ε_z (%)	Second scan ε_z (%)	Third scan ε_z (%)	Fourth scan ε_z (%)
SB	46.3	114.8	0	-7.8	-13.7	-23.5

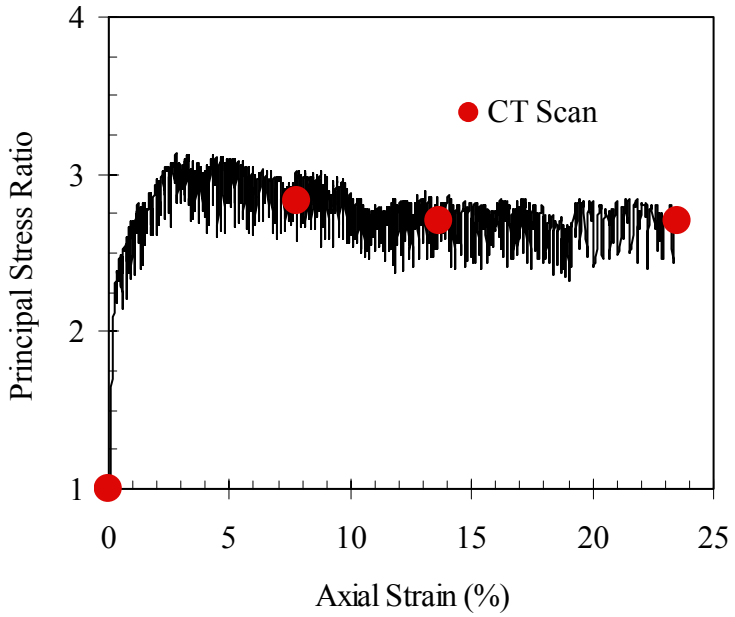

Figure 3.6. Axial strain versus principal stress ratio for the specimen

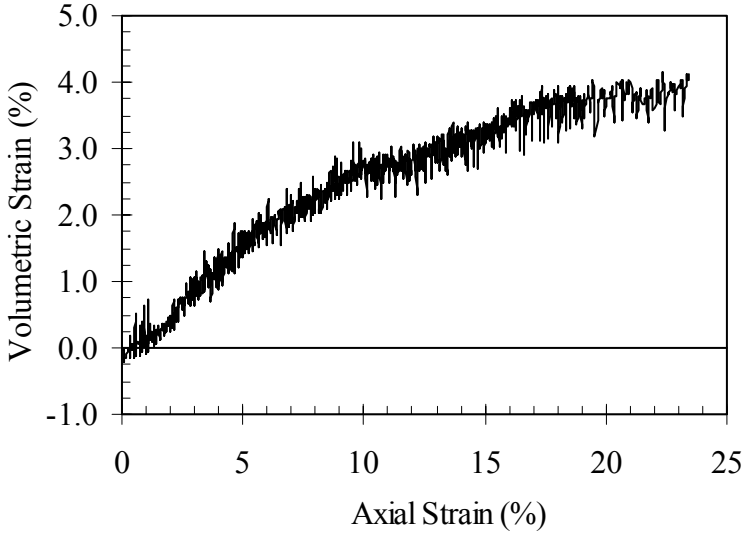

Figure 3.7. Axial strain versus volumetric strain for the specimen

3.3 VIEWING THE CT IMAGES AND DATA COLLECTION

The CT data was viewed using a powerful software package called FlashCT_VIZ, version 2.2, this software views the CT images one by one, or it can build a volume by stacking the cross sectional slices and view the whole volume at once, with different color and resolution options. Figure 3.8 shows an example cross sectional slice image with some aluminum wires, it can be seen that the aluminum can be clearly distinguished because of its higher attenuation coefficient. The quality of the images was very good, with no noticeable artifacts, and a high special resolution of 0.111 mm/pixel. Figure 3.9 shows the volume renderings of the specimen.

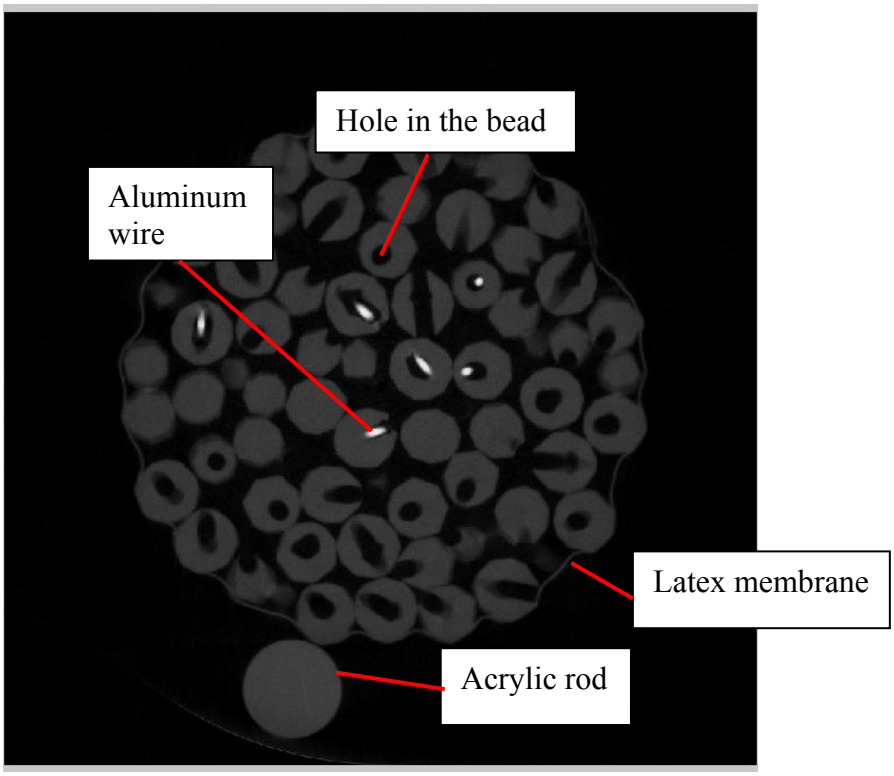

Figure 3.8. Example CT slice

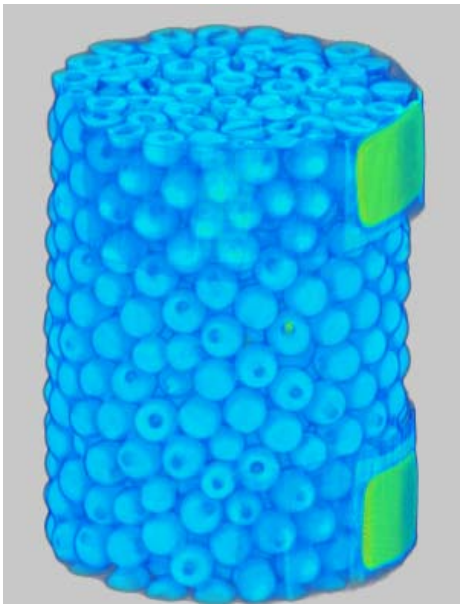

(a) $\varepsilon_z = 0\%$

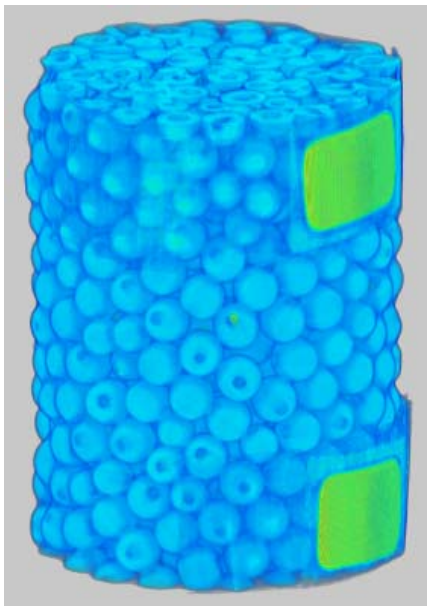

(b) $\varepsilon_z = -7.8\%$

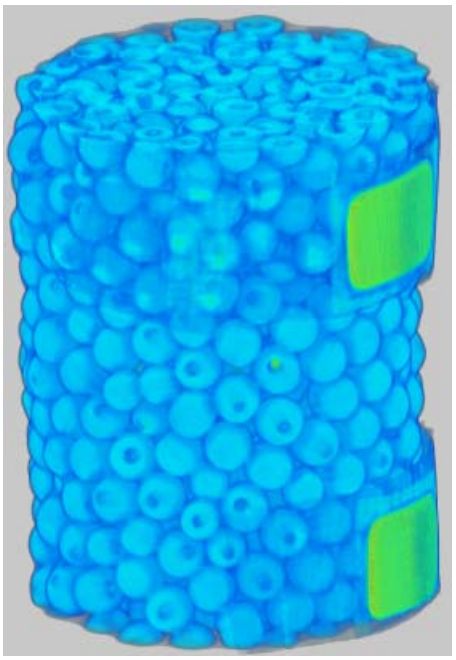

(c) $\varepsilon_z = -13.7\%$

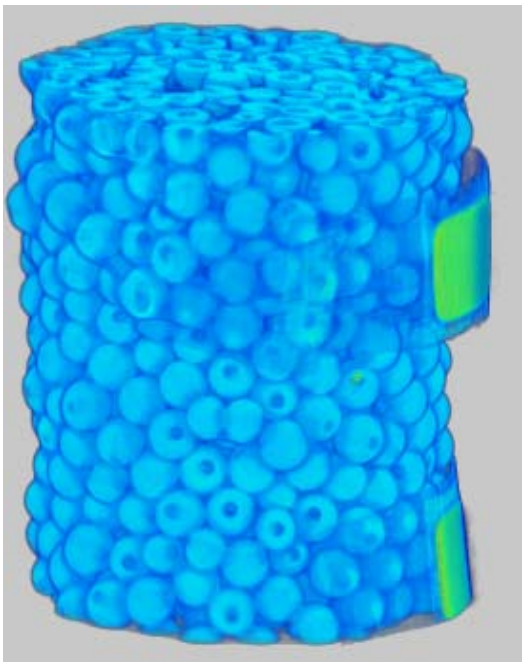

(d) $\varepsilon_z = -23.5\%$

Figure 3.8. CT volume renderings of the specimen

The next step is to track the locations of each particle throughout the four scans; this is a tedious process that requires a lot of time because it had to be done manually. Since, human judgment was needed in this process, writing a computer program to perform this job was not a feasible option. First, cross sections that have the same particles must be identified in the four volumes; this is achieved by marking a small formation of particles in one scan, and searching the other scans for a similar formation. And then, particles are numbered such that the same particle has the same number in the four scans. Figure 3.10 shows four cross sections containing the same particles taken from four different scans, and the numbering of the particles in each cross section. Then, the coordinates of the air hole (or the aluminum wire) in each hole must be recorded. The air hole of each particle is followed by stepping through consecutive slices until the end point is identified. The x, y and z coordinates of the end point were recorded. Then, coordinates of the other end point of the particle were identified following the same procedure. The accuracy of the recorded coordinates is checked by calculating the distance between the end points of the particle; the distance should be equal to the diameter of the particle. This procedure was performed for nearly all the particles in the scanned volume (400 particles) to be able to perform an accurate statistical analysis on the results.

- **Translation and Rotation Calculations**

The coordinates of the centroid of a particle were calculated as the mean value of its hole start and end coordinates. Having the coordinates of the center of the particle in the four scans, the translation in any direction can be calculated as the difference between the location of the centroid in one scan, and its location in the other scans (Equations 3.1 – 3.3), and the total distance traveled by the particle can be calculated using Equation 3.4.

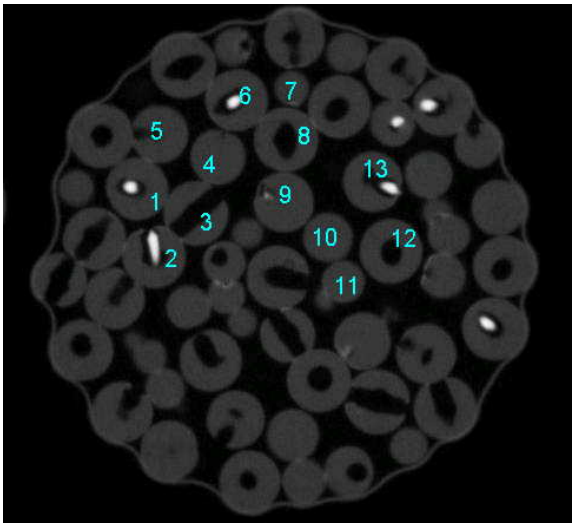

(a) $\varepsilon_z = 0\%$

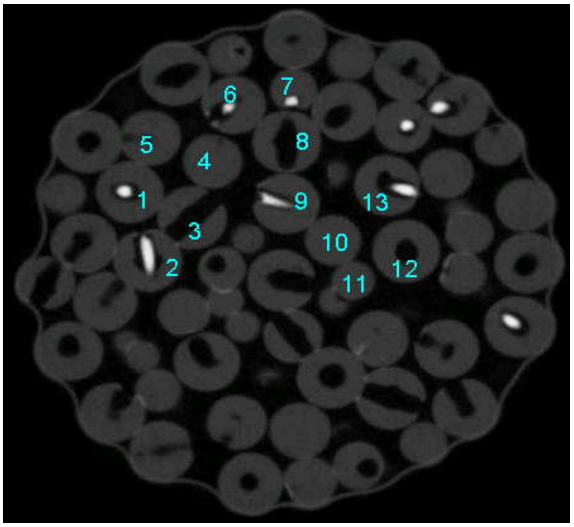

(b) $\varepsilon_z = -7.8\%$

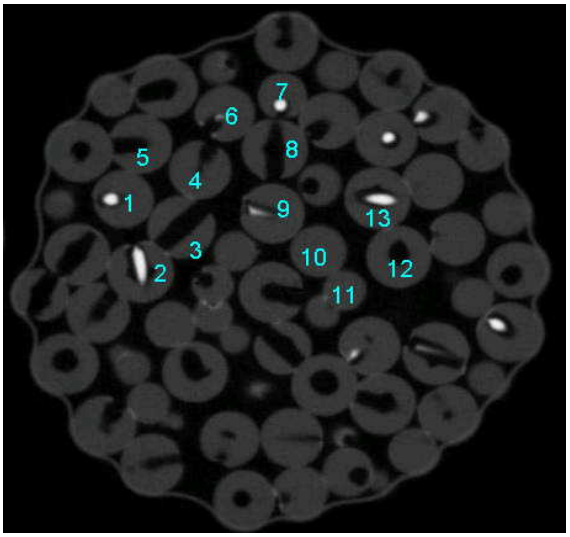

(c) $\varepsilon_z = -13.7\%$

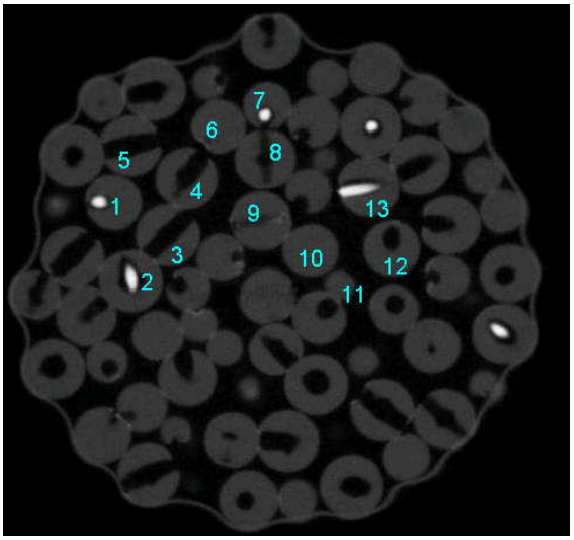

(d) $\varepsilon_z = -23.5\%$

Figure 3.10. Locating the particles in different cross sections and labeling them

$\Delta x = x_{(scan\ 2)} - x_{(scan\ 1)}$ ..... (3.1)

$\Delta y = y_{(scan\ 2)} - y_{(scan\ 1)}$ ..... (3.2)

$\Delta z = z_{(scan\ 2)} - z_{(scan\ 1)}$ ..... (3.3)

$D = \sqrt{\Delta x^2 + \Delta y^2 + \Delta z^2}$ ..... (3.4)

The rotation of each particle was calculated using spherical coordinates system. A local coordinate system was implemented for each particle. The center of the local coordinate system is located at the center of the particle, and (r) is the radius of the particle (Figure 3.11). In spherical coordinates, one can write:

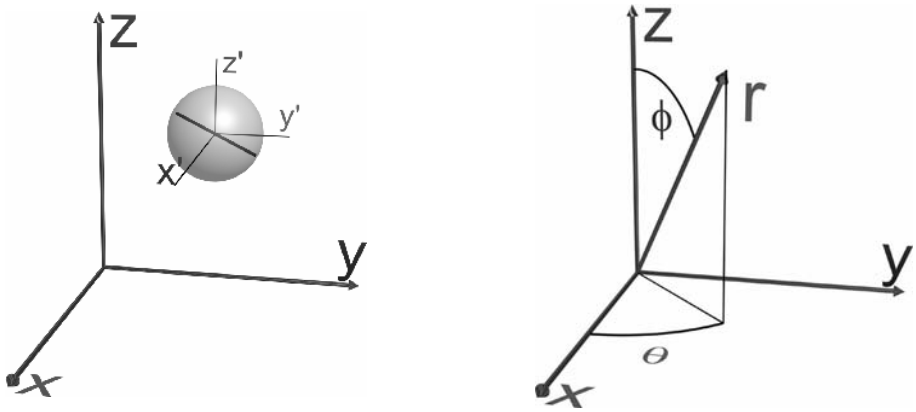

(a) (b)

Figure 3.11. (a) Global and local coordinates, (b) Spherical coordinates

$x = r \sin\phi \cos\theta$ ..... (3.5)

$y = r \sin\phi \sin\theta$ ..... (3.6)

$z = r \cos\phi$ ..... (3.7)

The values of ϕ and θ can be calculated using Equations (3.8 and 3.9).

$\phi = \cos^{-1} \frac{z}{r}$ ..... (3.8)

$$\theta = \tan^{-1}\frac{y}{x} \qquad \text{..... (3.9)}$$

The rotation of the particles was taken to be the change in ϕ and θ angles, where the change in ϕ is considered to be the vertical component of the rotation, and the change in θ is the horizontal component of the rotation.

- **Local strains**

Wang et al. (1999) proposed a finite element based approach to calculate the local strains resulting from rutting in asphalt concrete. 2D digital images of predefined cross sections were used to compare the positions of aggregates at different loading levels. A similar method was used to calculate the local strains in the beads specimen. Modifications were introduced to account for the third dimension, since, unlike digital images, 3D data is obtained during the CT scanning process.

The finite element definition of a linear displacement field is presented in Equations 3.10 through 3.12.

$$u = a_0 + a_1 x + a_2 y + a_3 z \qquad \text{..... (3.10)}$$

$$v = b_0 + b_1 x + b_2 y + b_3 z \qquad \text{..... (3.11)}$$

$$w = c_0 + c_1 x + c_2 y + c_3 z \qquad \text{..... (3.12)}$$

Where: u = the displacement in the x direction.

v = the displacement in the y direction.

w = the displacement in the z direction.

x,y,z = the coordinates of the point in the image.

This definition of the displacement field was used to describe the displacement of the particles in the specimen. u is equal to Δx, v is equal to Δy, w is equal to Δz. x,y,z were taken as

the coordinates of the centroid of the particle. Four coefficients are present in each Equation, therefore, four particles were considered each time to represent the initial condition. This was done by selecting the three closest particles (j,k,l) to particle (i). Distances from the center of particle (i) to the centers of all the other particles were calculated using Equation (3.4). Then the closest three particles were selected as the particles with the minimum distances from the center of particle (i). Having the coordinates and displacements of four particles, the system of equations can be written in a matrix form (Equation 3.13).

$$\begin{pmatrix} 1 & x_i & y_i & z_i \\ 1 & x_j & y_j & z_j \\ 1 & x_k & y_k & z_k \\ 1 & x_l & y_l & z_l \end{pmatrix} \cdot \begin{pmatrix} a_0 \\ a_1 \\ a_2 \\ a_3 \end{pmatrix} = \begin{pmatrix} u_i \\ u_j \\ u_k \\ u_l \end{pmatrix} \quad \text{..... (3.13)}$$

Where, x,y and z denote the coordinates of the centroid; i,j,k and l denote particles.

This system was solved to obtain the "a" coefficients. Then, the same procedure was repeated to calculate the "b" and "c" coefficients using the v and w displacement fields, respectively. A computer program was written using MATHCAD software to perform this analysis. The input for the program was the coordinates of the centroid of all particles in two scans. For every particle, the distances from the centroids of all the other particles to the centroid of the particle are calculated, and the closest three particles are selected. Systems of equations similar to the one presented in Equation (3.13) were solved for the a`s , b`s , and c`s.

The program calculates the strain values using Equations (3.14 – 3.22). This procedure is repeated for all the particles in the volume, yielding a large number of local strain values that allows for performing a representative statistical analysis for the local strains distributions.

$$\varepsilon_x = \frac{\partial u}{\partial x} = a_1 \quad \text{..... (3.14)}$$

$$\varepsilon_y = \frac{\partial v}{\partial y} = b_2 \quad \text{.....(3.15)}$$

$$\varepsilon_z = \frac{\partial w}{\partial z} = c_3 \quad \text{.....(3.16)}$$

$$\varepsilon_{xy} = \frac{\left(\frac{\partial u}{\partial y} + \frac{\partial v}{\partial x}\right)}{2} = \frac{a_2 + b_1}{2} \quad \text{.....(3.17)}$$

$$\varepsilon_{xz} = \frac{\left(\frac{\partial u}{\partial z} + \frac{\partial w}{\partial x}\right)}{2} = \frac{a_3 + c_1}{2} \quad \text{.....(3.18)}$$

$$\varepsilon_{yz} = \frac{\left(\frac{\partial v}{\partial z} + \frac{\partial w}{\partial y}\right)}{2} = \frac{b_3 + c_2}{2} \quad \text{.....(3.19)}$$

$$\omega_{xy} = \frac{\left(\frac{\partial u}{\partial y} - \frac{\partial v}{\partial x}\right)}{2} = \frac{a_2 - b_1}{2} \quad \text{.....(3.20)}$$

$$\omega_{xz} = \frac{\left(\frac{\partial u}{\partial z} - \frac{\partial w}{\partial x}\right)}{2} = \frac{a_3 - c_1}{2} \quad \text{.....(3.21)}$$

$$\omega_{yz} = \frac{\left(\frac{\partial v}{\partial z} - \frac{\partial w}{\partial y}\right)}{2} = \frac{b_3 - c_2}{2} \quad \text{.....(3.22)}$$

After calculating all the strain components, the local dilatancy angles (θ) can be calculated as (Tatsuoka, 1987):

$$\psi_l = \sin^{-1}\left(-\frac{\varepsilon_1 + 2\varepsilon_3}{\varepsilon_1 - 2\varepsilon_3}\right) \quad \text{..... (3.23)}$$

Where ε_1 and ε_3 are the major and minor principle stresses calculated from the strain tensor ε_{ij}.

Tatsuoka (1987) suggested Equation (3.23) for axisymmetric triaxial compression based on comparison of $(d\varepsilon_v / d\varepsilon_1)$ laboratory measurements of plane strain and axisymmetric triaxial compression experiments.

- **3D Visualization**

After obtaining the coordinates of all the particles, they were used to generate 3D renderings of the particles. Figures 3.12 through 3.15 show multiple views of a cluster of eight particles at four different compression stages. And Figures 3.16 through 3.18 show multiple views on individual beads at the four compression stages. It is also possible to create 3D animations showing the movement of the particles throughout the experiment.

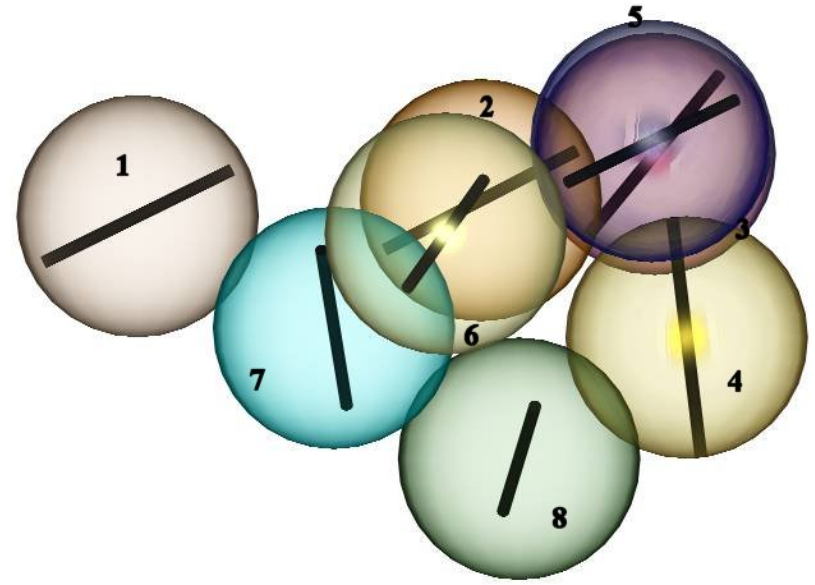

(a) x-z view (front view)

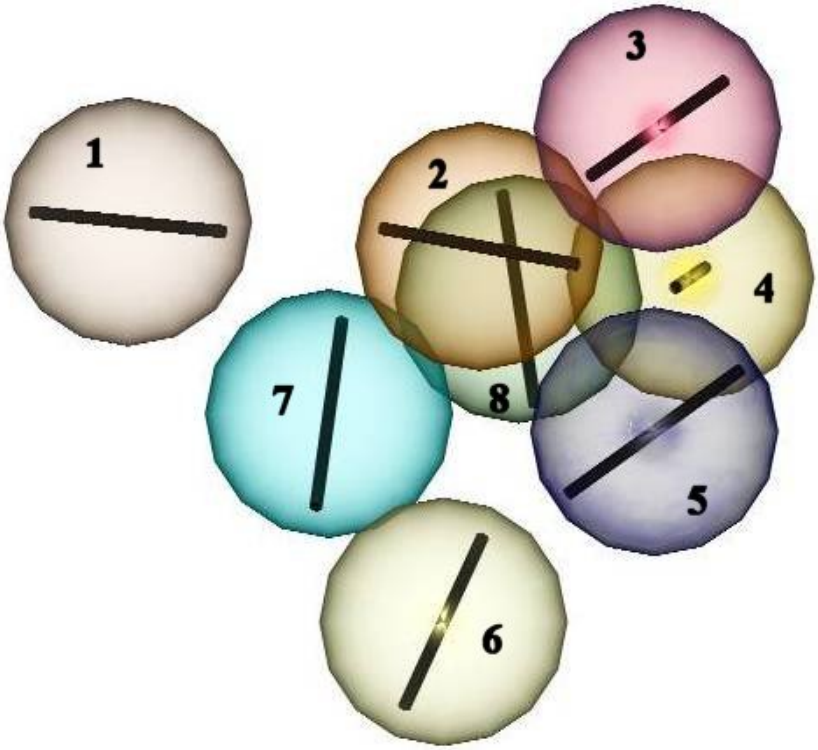

(b) x-y view (top view)

Figure 3.12. 3D rendering of a cluster of particles before compression (ε_z = 0%)

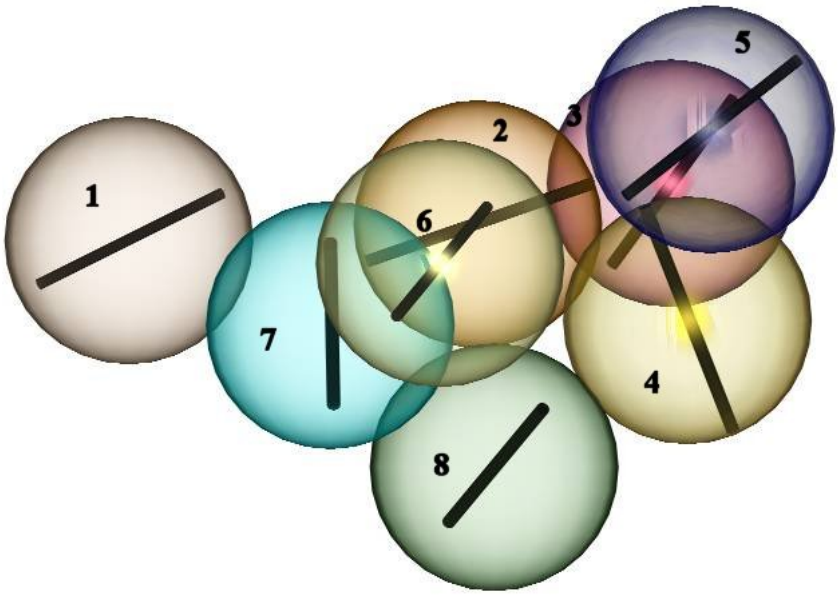

(a) x-z view (front view)

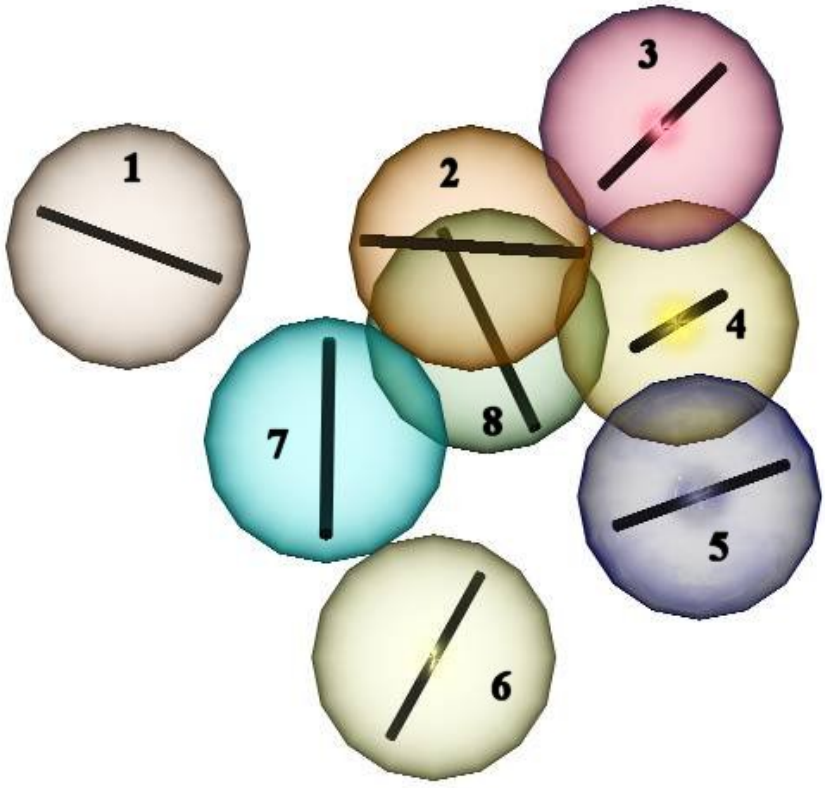

(b) x-y view (top view)

Figure 3.13. 3D rendering of a cluster of particles at ε_z = -7.8%

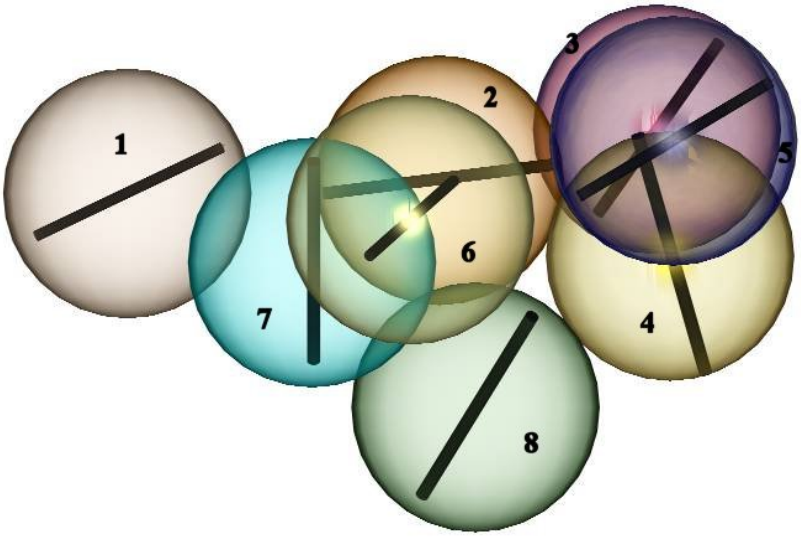

(a) x-z view (front view)

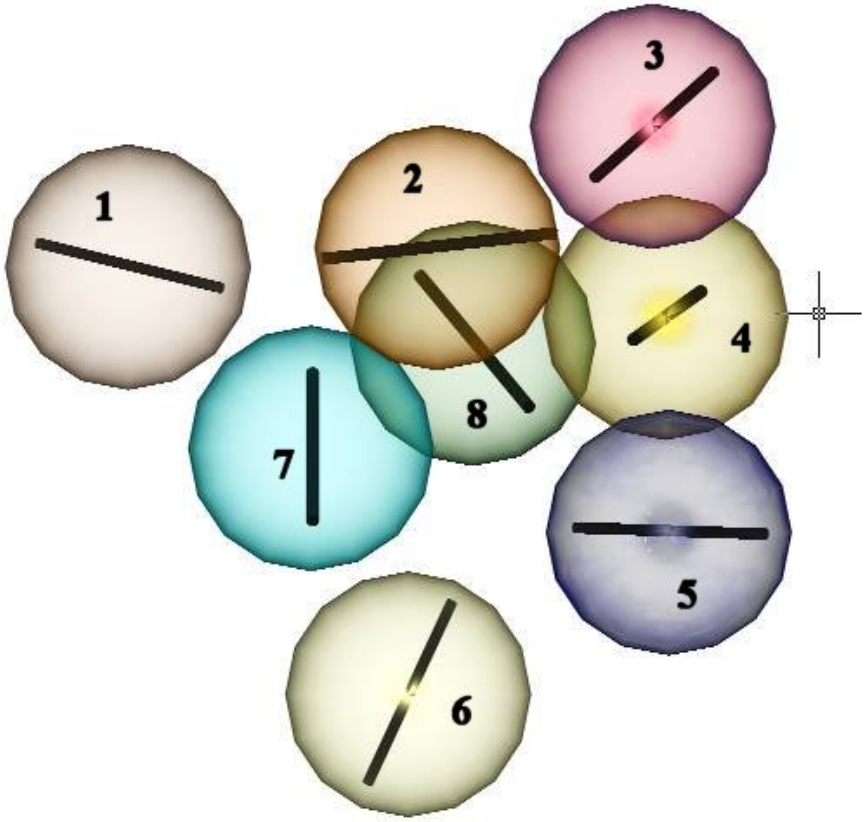

(b) x-y view (top view)

Figure 3.14. 3D rendering of a cluster of particles at ε_z = -13.7%

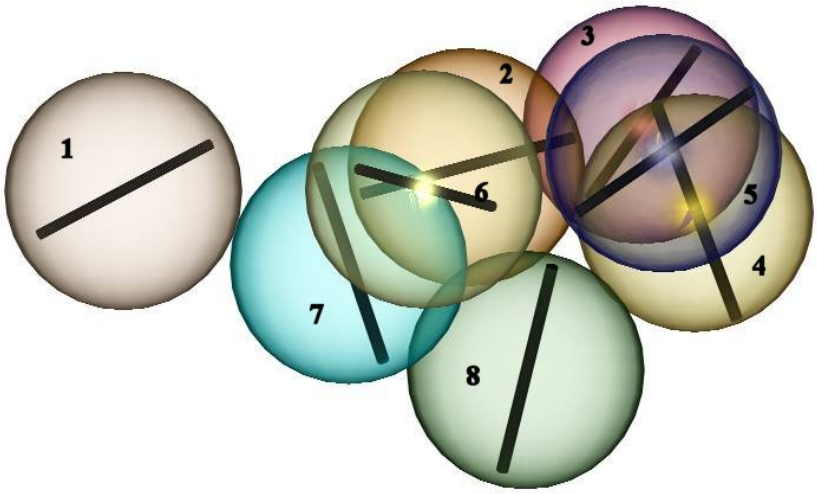

(a) x-z view (front view)

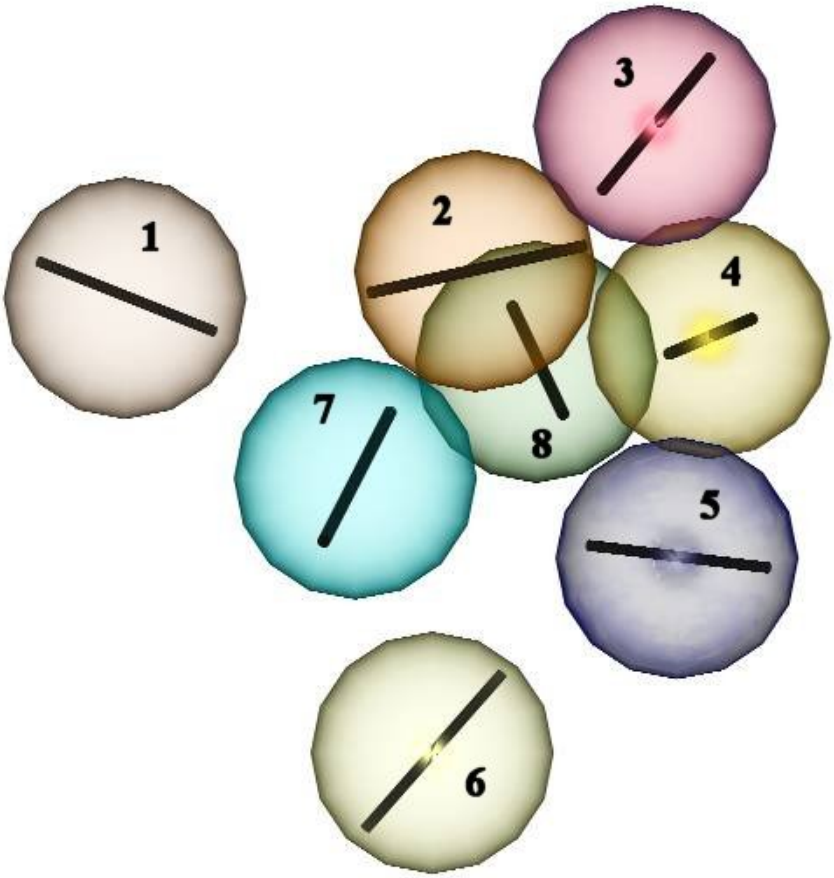

(b) x-y view (top view)

Figure 3.15. 3D rendering of a cluster of particles at ε_z = -23.5%

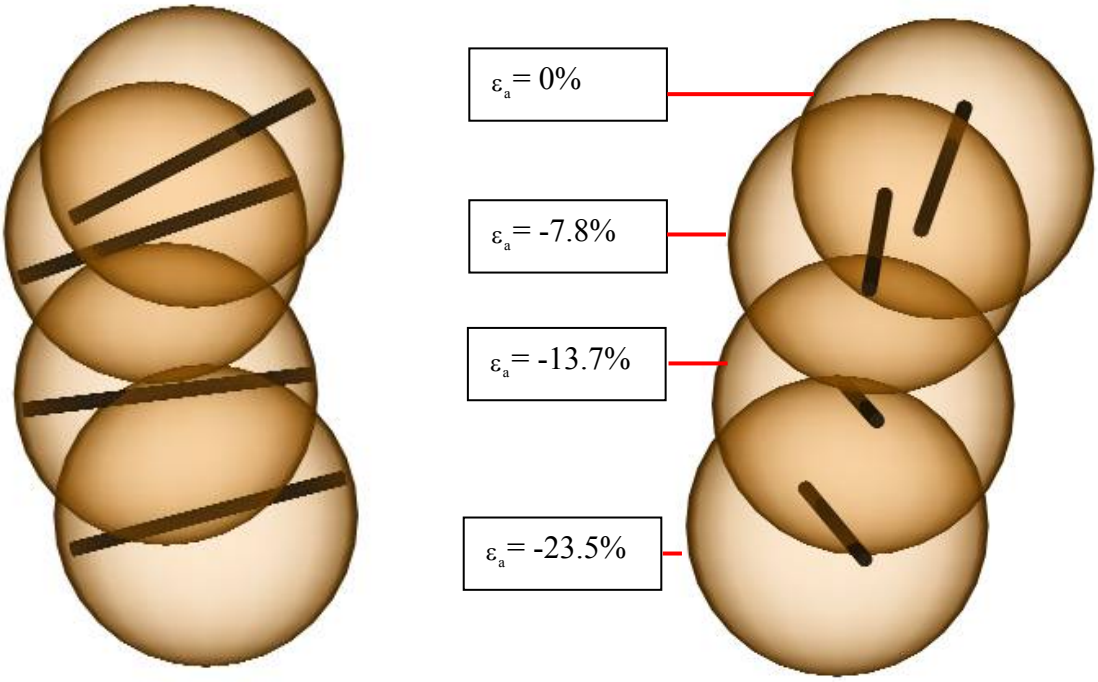

(a) x-z view (front view) (b) y-z view (side view)

Figure 3.16. Sequence of movement of Bead 2 at the four compression stages

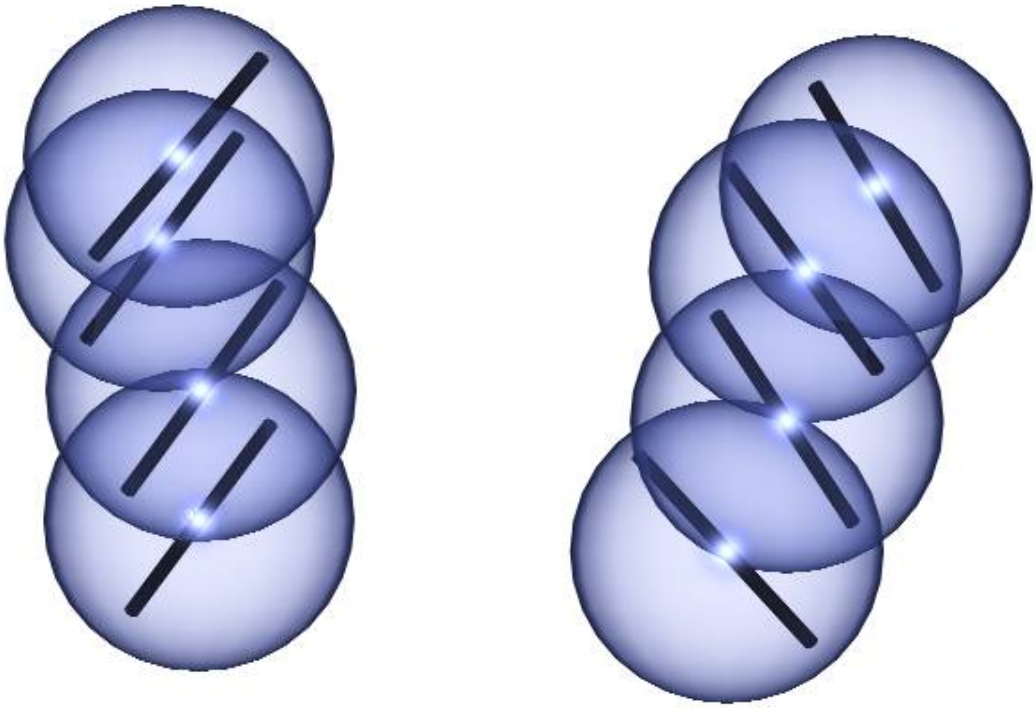

(a) x-z view (front view) (b) y-z view (side view)

Figure 3.17. Sequence of movement of Bead 2 at the four compression stages

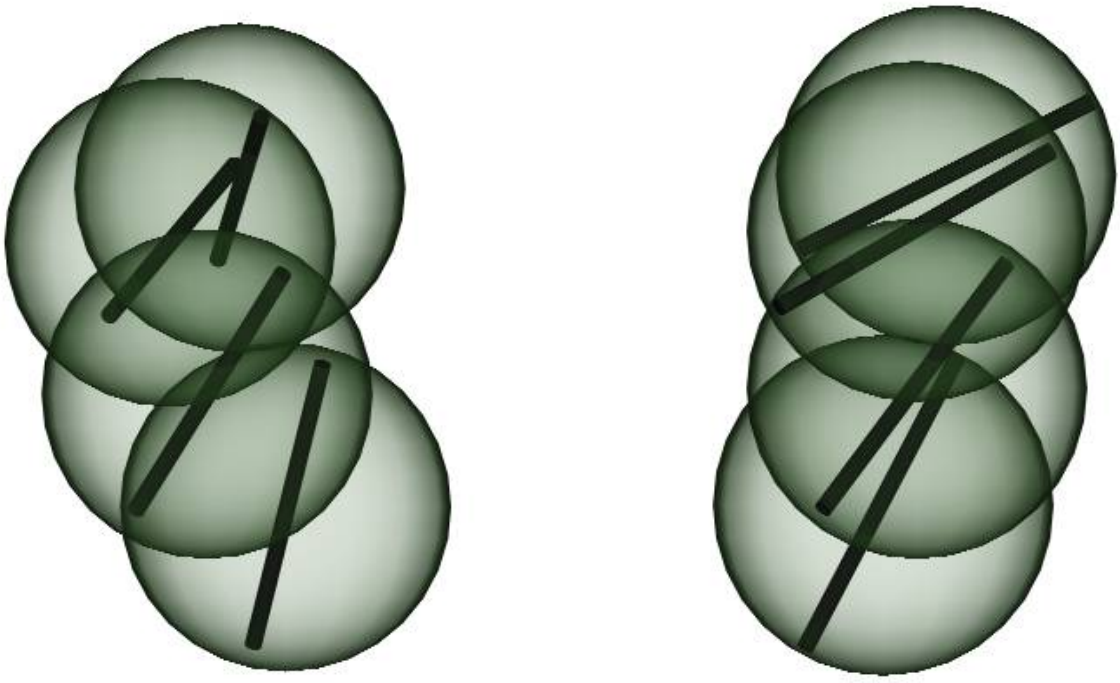

(a) x-z view (front view) (b) y-z view (side view)

Figure 3.18. Sequence of movement of Bead 8 at the four compression stages

CHAPTER FOUR

RESULTS AND DISCUSSION

4.1 RESULTS

4.1.1 Translation and Rotation

The translation and rotation for four hundred particles were calculated as described in Chapter 3. The data was presented in the form of frequency distributions. A statistical analysis was performed, and the data was then fitted to the closest probability density distribution. Then the "90% level of confidence" intervals were calculated.

- **Translation**

The Frequency distributions for the translation for the first stage of the experiment are presented in Figure 4.1, and for the other stages, the figures are presented in Appendix A. Since the scanning was not performed on uniform strain intervals, the translation values were normalized with respect to the value of the displacement at the top of the specimen at every stage of the experiment, and are presented as percentages of that value. It should be noted that the translation values are not presented in cumulative form, i.e. the presented values represent the translation that took place between the scan under consideration, and the previous scan. This way of presentation was selected to make it easier to note the changes in the translation rate that takes place at different stages throughout the experiment. The values for the horizontal translations (X and Y directions) were taken as absolute values.

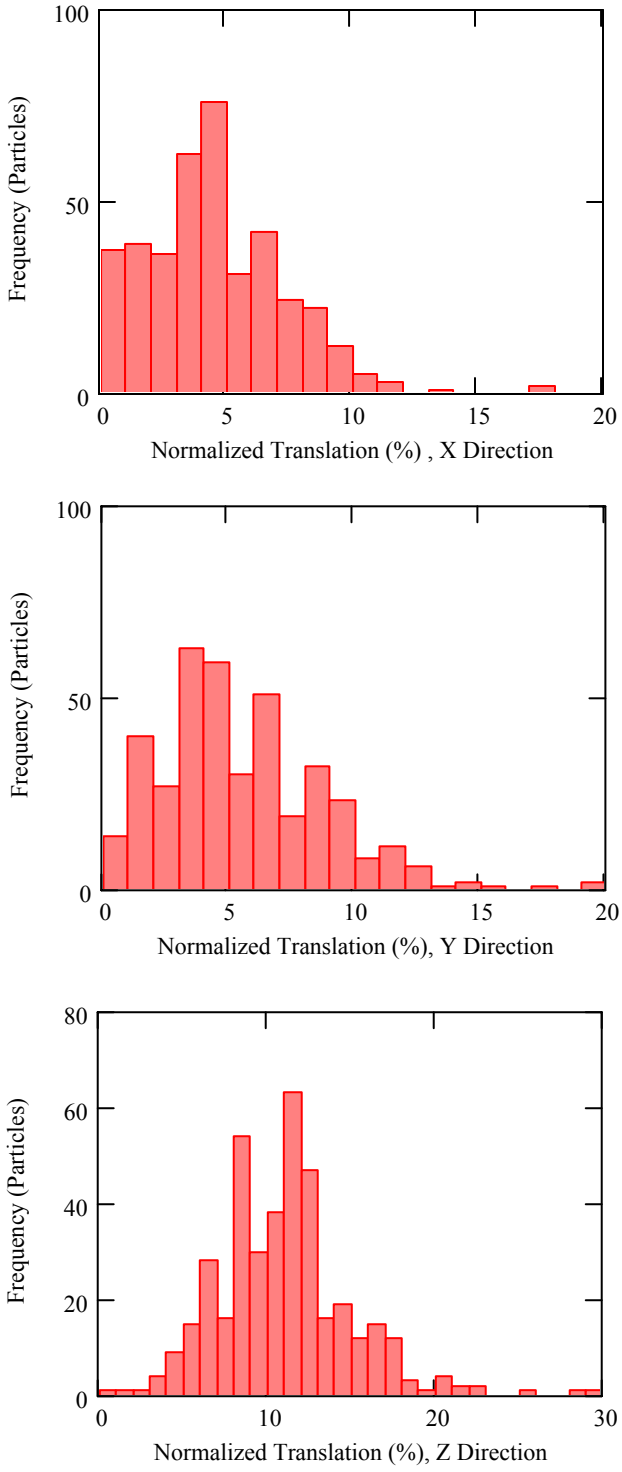

Figure 4.1: Normalized Translation Histograms at ε_z = -7.8 %
(Normalization Value = 9 mm)

Table 4.1 summarizes the results of the translation values throughout the experiment, and the type of the probability distribution that best fits the data. It also presents the lower limit (L) of the 90% confidence interval (CI) where 5% of the values are less than or equal to this value, and the upper limit (U) of the 90% confidence interval where 95% of the values are less than or equal to this value. The 90% CI is the interval lying between L and U, where 90% of the sample lies.

Table 4.1. Summary of normalized translation data and distribution fitting

Global ε_z (%)	Direction	Actual Data		Statistical Fit					
		Mean (%)	St. Dev. (%)	Distribution	Mean (%)	St. Dev. (%)	L (%)	U (%)	90% CI
-7.8	X	5.32	4.673	Log-Normal	4.11	2.72	0	8.72	8.72
	Y	6.47	6.44	Log-Normal	5.47	3.38	0.89	11.71	10.82
	Z	11.25	4.50	Log-Normal	10.68	3.42	5.14	16.4	11.26
-13.7	X	7.93	6.24	Beta	8.12	6.06	0.99	20.16	19.1
	Y	6.5	6.66	Weibull	4.61	3.60	0	11.35	11.35
	Z	20.97	8.59	Log-Normal	20.21	8.03	7.01	33.43	26.42
-23.5	X	9.88	7.77	Beta	8.23	6.50	0.73	21.25	20.52
	Y	8.84	7.75	Beta	7.46	5.51	0.61	19.01	18.4
	Z	24.27	8.96	Log-Normal	26.138	9.27	14.08	43.43	29.35

- **Rotation**

As mentioned earlier, using spherical coordinates, two rotation angles were considered, represented by ϕ and θ. The frequency distributions for the rotation throughout the experiment are illustrated in Figures 4.2 and 4.3.The the rotation data are presented in a cumulative form. To show the total amount of rotation that the particles undergo, the Figures show the sum of the absolute values of the rotations taking place throughout the experiment. A summary of the results along with the statistical data and distribution fitting for the rotations is presented in Tables 4.2 and 4.3.

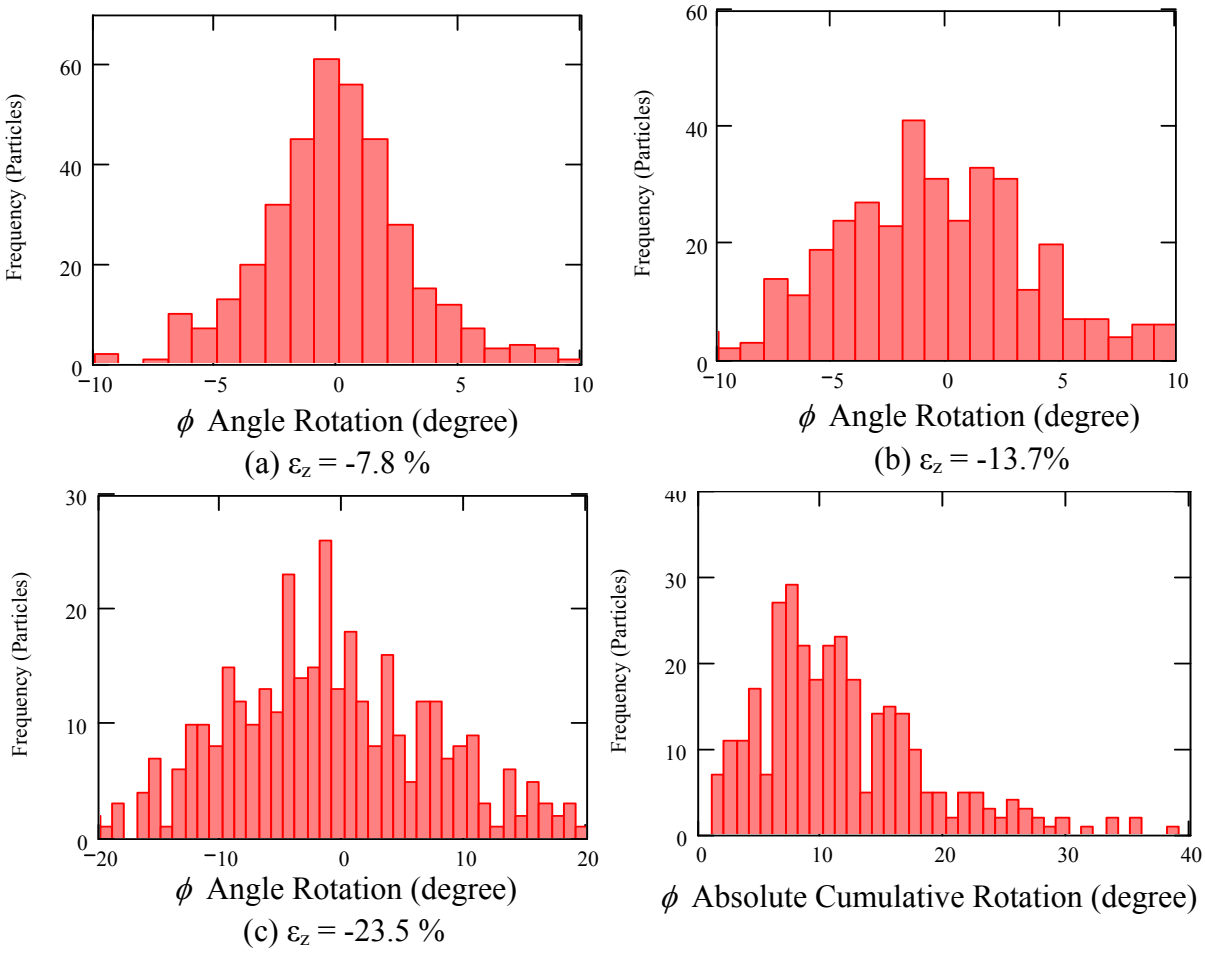

Figure 4.2. ϕ Angle rotation throughout the experiment

Table 4.2. Statistical summary of rotation angle ϕ

ε_z (%)	Actual Data		Statistical Fit					
	Mean (degree)	Std. Dev (degree)	Distribution	Mean (degree.)	St. Dev. (degree)	L (degree.)	U (degree.)	90% CI (degree)
-7.8	-0.074	4.74	Normal	-0.13	2.93	-4.89	4.62	9.51
-13.7	-0.93	8.79	Normal	-0.76	4.67	-8.40	6.90	15.3
-23.5	-2.34	11.46	Normal	-2.00	11.46	-17.10	13.09	30.19

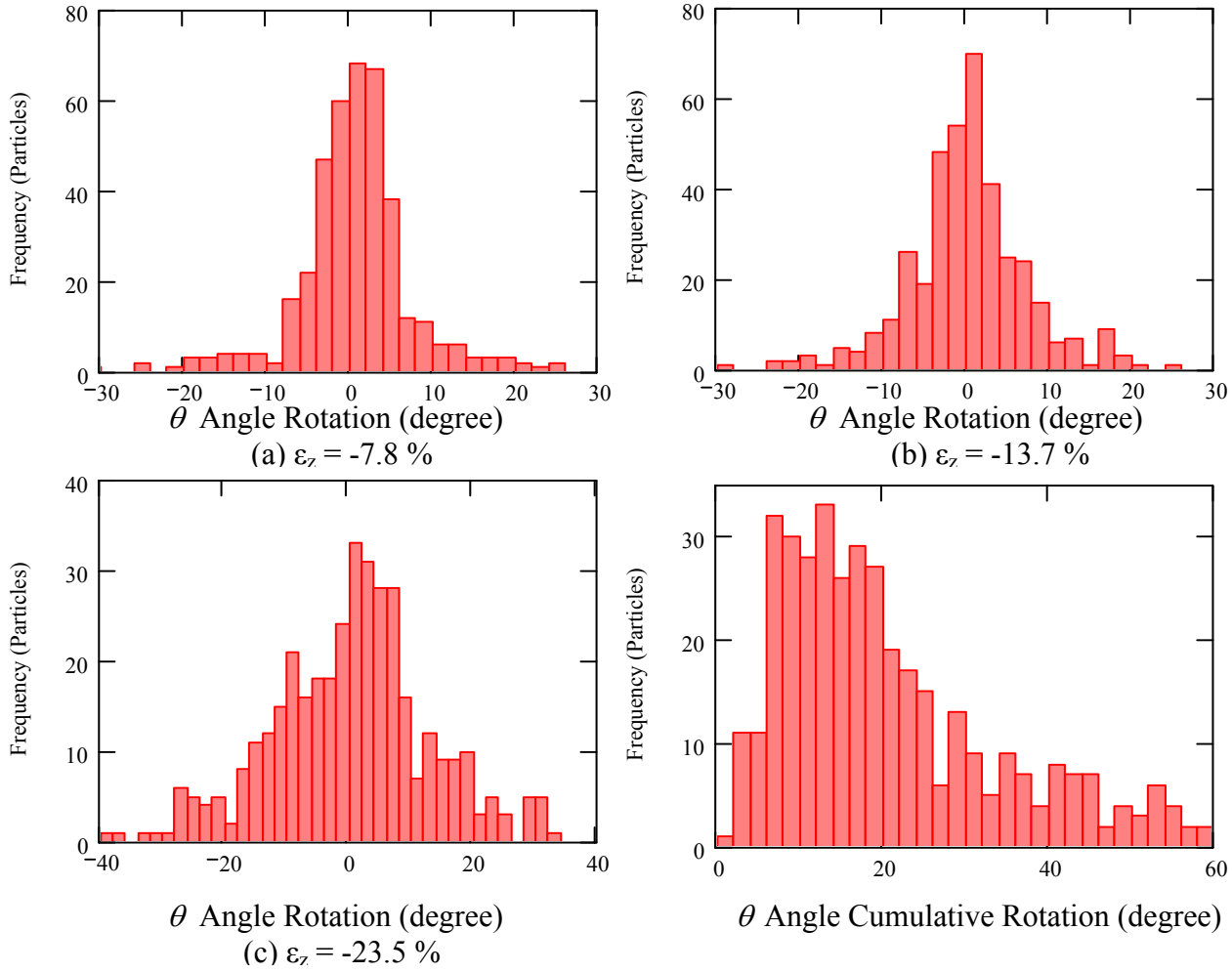

Figure 4.3: θ angle rotation throughout the experiment

Table 4.3: Statistical summary of rotation angle θ

ε_z (%)	Actual Data		Statistical Fit					
	Mean (degree.)	Std. Dev (degree)	Distribution	Mean (degree)	St. Dev. (degree)	L (degree)	U (degree)	90% CI (degree)
-7.8	0.51	7.63	Normal	0.75	4.91	-7.22	8.73	15.95
-13.7	1.16	11.92	Normal	0.69	7.60	-11.8	13.2	25
-23.5	1.66	20.85	Normal	1.46	16.26	-25.3	28.2	53.5

4.1.2 Local Strains

The local strains are calculated using the method described in the previous Chapter (Equations 3.14 through 3.22). The results for the first stage of the experiment are presented in

Figures 4.4 and 4.5 in the form of frequency distributions, and the results for the following stages are presented in Appendix B. Cumulative values of the axial and radial strains (ε_z, ε_x and ε_y), shear strains (ε_{xy}, ε_{xz}, and ε_{yz}), and rotation strains(ω_{xy}, ω_{xz}, and ω_{yz}) at the different stages on the experiment are presented in each Figure. Then a summary of the results along with the best fit frequency distribution and the confidence intervals are shown in Tables 4.4, 4.5 and 4.6.

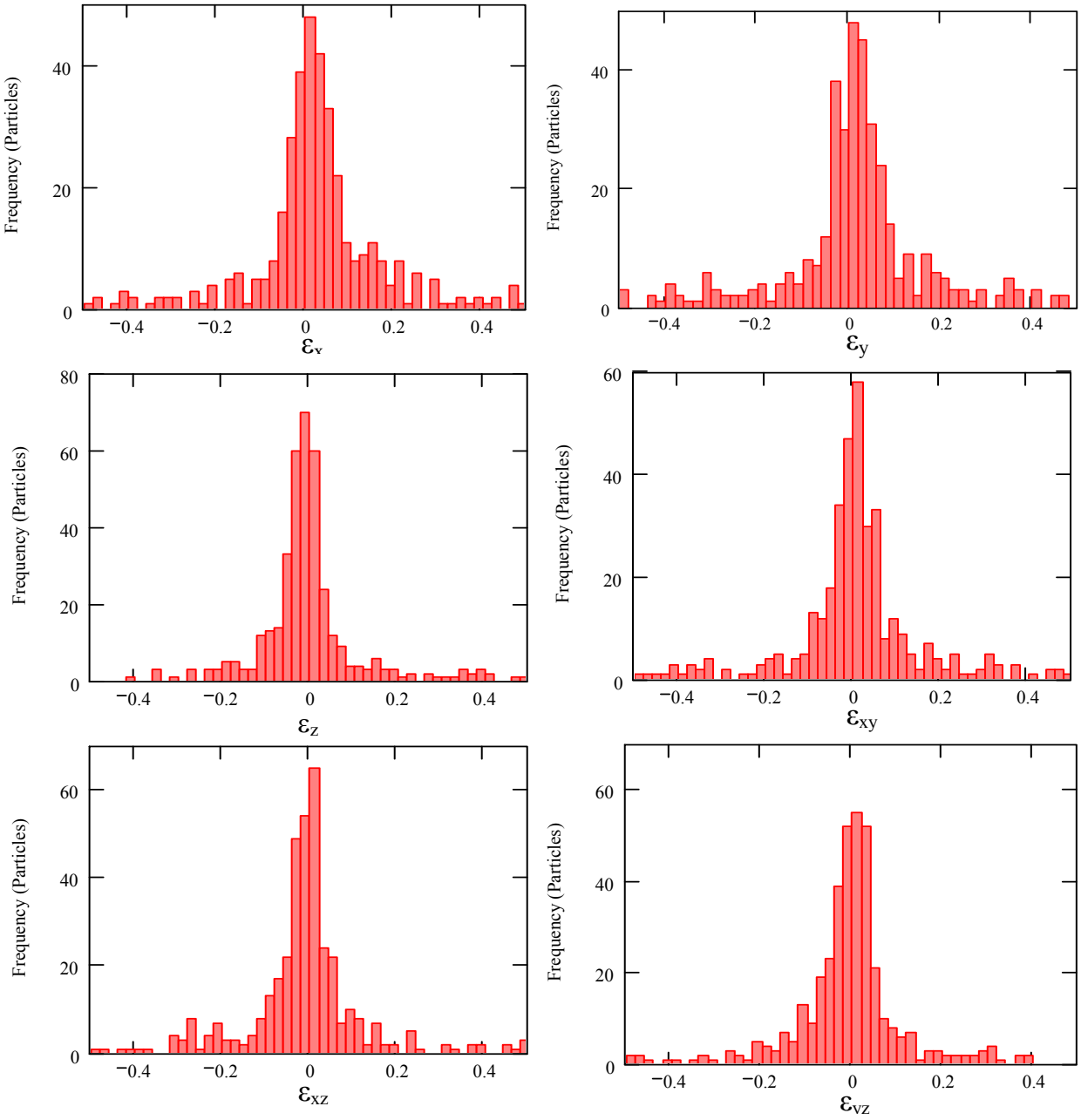

Figure 4.4. Local strains histograms at ε_z = -7.8%

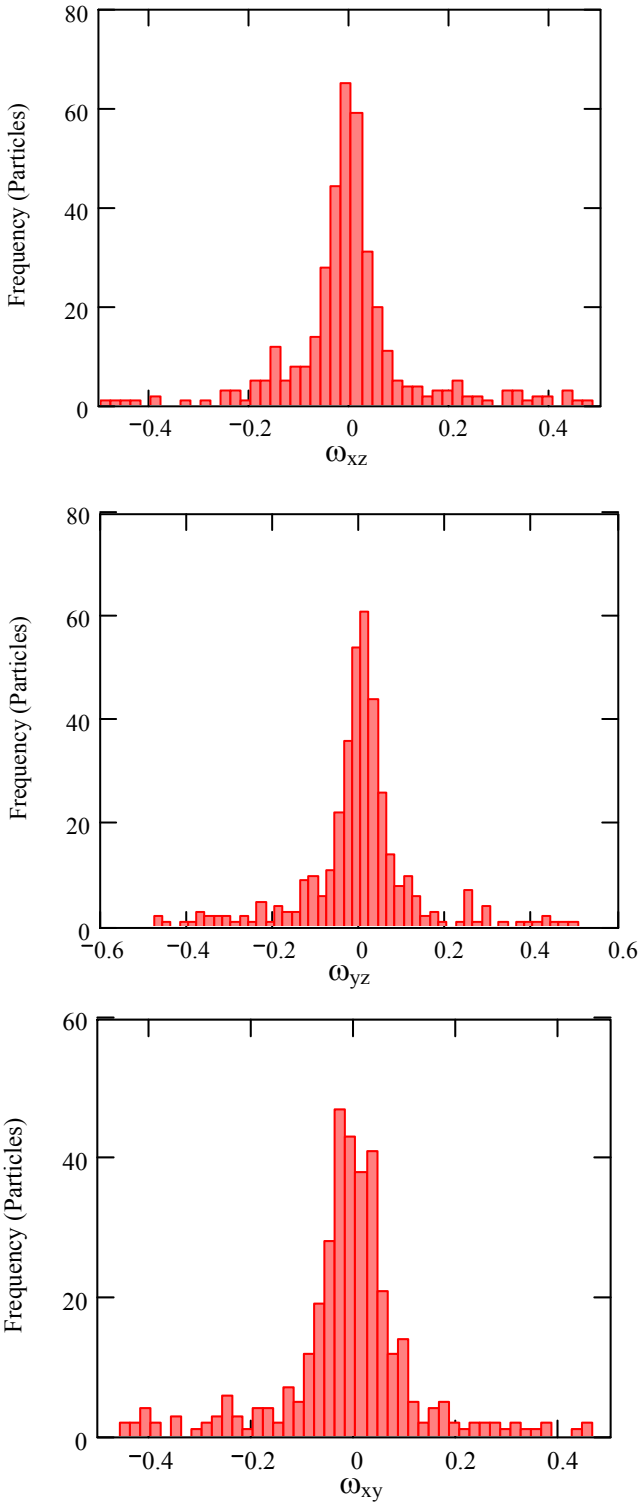

Figure 4.5. Rotation strains histograms at ε_z = -7.8%

Table 4.4: Summary of axial and radial strains data and distribution fitting

Global ε_z (%)	Component	Actual Data		Statistical Fit					
		Mean	St. Dev.	Distribution	Mean	St. Dev.	L	U	90% CI
-7.8	ε_x	0.026	0.15	Log-Normal	0.065	0.10	-0.045	0.262	0.307
	ε_y	0.014	0.15	Log-Normal	0.089	0.15	-0.037	0.359	0.396
	ε_z	-0.014	0.08	Normal	-0.013	0.04	-0.080	0.055	0.135
-13.7	ε_x	0.041	0.16	Log-Normal	0.056	0.12	-0.115	0.275	0.390
	ε_y	0.035	0.15	Log-Normal	0.053	0.10	-0.089	0.223	0.312
	ε_z	-0.016	0.14	Normal	0.012	0.06	-0.115	0.09	0.205
-23.5	ε_x	0.085	0.32	Log-Normal	0.133	0.26	-0.240	0.611	0.851
	ε_y	0.070	0.36	Log-Normal	0.140	0.27	-0.244	0.621	0.865
	ε_z	0.002	0.39	Logistic	-0.049	0.19	-0.358	0.259	0.617

Table 4.5: Summary of shear strains data and distribution fitting

Global ε_z (%)	Component	Actual Data		Statistical Fit					
		Mean	St. Dev.	Distribution	Mean	St. Dev.	L	U	90% CI
-7.8	ε_{xy}	0.006	0.14	Logistic	0.003	0.07	-0.104	0.111	0.215
	ε_{xz}	-0.013	0.13	Logistic	-0.006	0.06	-0.101	0.088	0.189
	ε_{yz}	-0.007	0.12	Logistic	0.000	0.06	-0.100	0.100	0.200
-13.7	ε_{xy}	0.010	0.16	Logistic	0.01	0.09	-0.133	0.150	0.283
	ε_{xz}	-0.002	0.15	Logistic	-0.008	0.09	-0.152	0.136	0.288
	ε_{yz}	-0.001	0.14	Logistic	0.007	0.09	-0.143	0.156	0.299
-23.5	ε_{xy}	0.036	0.35	Logistic	0.031	0.27	-0.409	0.472	0.881
	ε_{xz}	0.002	0.36	Logistic	-0.015	0.25	-0.429	0.398	0.827
	ε_{yz}	0.020	0.38	Logistic	0.003	0.27	-0.429	0.435	0.864

Table 4.6: Summary of rotation strains data and distribution fitting

Global ε_z (%)	Component	Actual Data		Statistical Fit					
		Mean	St. Dev.	Distribution	Mean	St. Dev.	L	U	90% CI
-7.8	ω_{xy}	-0.015	0.13	Logistic	-0.006	0.07	-0.121	0.109	0.230
	ω_{xz}	-0.001	0.13	Logistic	-0.006	0.05	-0.094	0.083	0.177
	ω_{yz}	-0.003	0.13	Logistic	0.004	0.06	-0.092	0.100	0.192
-13.7	ω_{xy}	-0.022	0.15	Logistic	-0.020	0.11	-0.193	0.152	0.345
	ω_{xz}	-0.023	0.15	Logistic	-0.025	0.10	-0.173	0.123	0.296
	ω_{yz}	0.015	0.15	Logistic	0.012	0.12	-0.177	0.202	0.379
-23.5	ω_{xy}	-0.007	0.34	Logistic	-0.038	0.23	-0.419	0.342	0.761
	ω_{xz}	-0.018	0.38	Logistic	-0.054	0.30	-0.540	0.433	0.973
	ω_{yz}	0.046	0.40	Logistic	0.004	0.27	-0.431	0.438	0.869

4.1.3 Dilatancy Angles

The local dilatancy angles are calculated using Equation 3.23. Figure 4.6 shows the local dilatancy angle histograms at the different stages of the experiment. A statistical summary of the results as well as the statistical fit information are shown in Table 4.7.

4.2 DISCUSSION OF RESULTS

4.2.1 Translation

The translation values in the lateral direction (x and y) and axial direction (z) were studied with the aid of Figures 4.1, A1, and A2 (Appendix A) and Table 4.1. The lateral translation during the first stage of the experiment (ε_z = -7.8%) looks similar in the x and y directions, a mean value of 5.3% of the displacement at top of the specimen was obtained in the x direction, and a value of 6.5% was obtained in the y direction (Figure 4.1). It is also realized that the shapes of the histograms in x and y direction look similar. This is due to the axisymmetric conditions of the experiment.

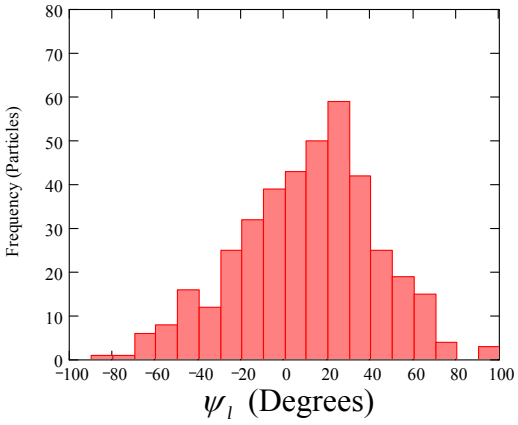

(a) ε_z = -7.8%

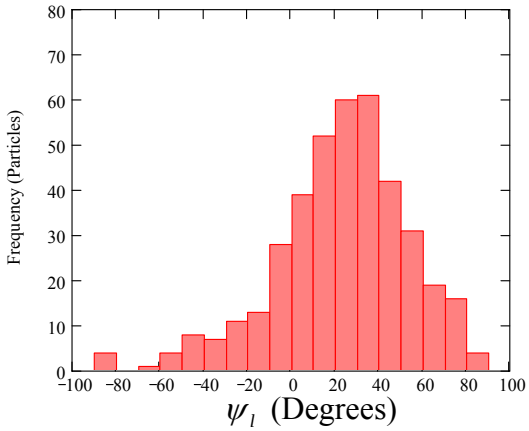

(b) ε_z = -13.7%

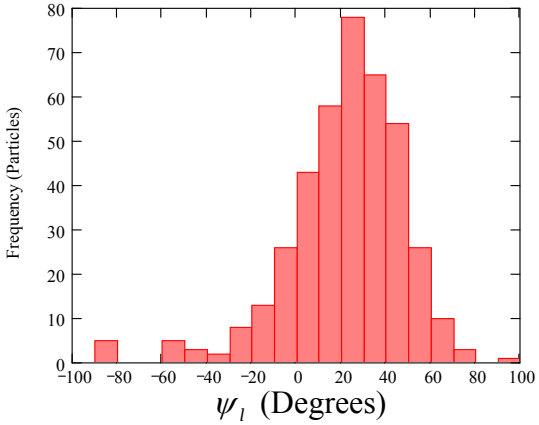

(c) ε_z = -23.5%

Figure 4.6: Local dilatancy angle histograms

Table 4.7: Summary of dilatancy angle data and distribution fitting

ε_z (%)	Actual Data		Statistical Fit					
	Mean (degree)	St. Dev. (degree)	Distribution	Mean (degree)	St. Dev. (degree)	L (degree)	U (degree)	90% CI (degree)
-7.8	10.19	31.9	Logistic	14.47	34.73	-41.9	70.8	112.7
-13.7	22.85	30.87	Logistic	26.87	29.93	-21.7	75.5	97.2
-23.5	21.68	26.53	Logistic	26.34	23.97	-12.6	65.3	77.9

On the other hand, looking at the values of translation in the z direction, the mean value was 11.25% of the displacement at the top of the specimen. It can be realized from the low value of standard deviation, and the shape of the histogram for the z direction translation, the homogeneity of the values of the axial distance traveled, where most of the values lie between 8% and 12%. The values of translation in the lateral and axial directions were relatively low, that can be explained that during the early stages of the experiment, the particles exhibit small rearrangement due to the application of stress on top of the specimen.

During the second stage of the experiment (Global ε_z = -13.5%) an increase in the rate of translation in the lateral direction was observed. The mean values for the translation were 7.93%, and 6.5% in the x and y directions, respectively (Figure A1). The mean value for the translation in the axial direction also increased to be 20.98%, which is about double the amount obtained in the first stage of the experiment. This increase in the translation values in the lateral and axial direction could be caused by the collapse of the large voids due to the continuous compression, causing higher translation value. Moreover, particles from the upper levels of the specimen migrate into the lower levels by displacing the underlying particles axially and laterally.

In the last stage of the experiment, (global ε_z = -23.5%), the translation in the lateral direction continues to increase, where the mean value for the translation in the x direction is 9.9%, and 8.84% in the y direction (Figure A2). It can be seen that the mean values in the x and y are still similar. Also, the similarity of the histograms of the translation in the x and y direction

can still be clearly seen where they both take the shape of a “Beta distribution”. As mentioned earlier, this is an expected result due the axisymmetric conditions of the experiment. The translation in the axial direction also increases, to have a mean value of 24.27% and the values in the 90% level of confidence reach up to 43%. This stage of the experiment is best described as the critical state, where the shear resistance of the specimen is very small and greater strains can be generated with relatively small stresses.

4.2.2 Rotation

As mentioned earlier, a vertical (ϕ) and a horizontal (θ) component of the rotation were considered. From Figure 4.2 and Table 4.2, the vertical rotation histograms during all the stages of the experiment take the shape of normal distributions. During the first stage of the experiment, 90% of the vertical rotation values lie between -4.9 and 4.6 degrees. While in the second stage they lie between -8.4 and 6.9 degrees. In the final stage of the experiment 90% of the values lie between -17.1 and 13.1 degrees. Taking the absolute values of all the rotations, the cumulative vertical rotation values reach up to 30 degrees. On the other hand, the horizontal rotation had higher values, where 90% of the values of the θ angle rotation in the first stage of the experiment range between -7.22 and 8.73 degrees (Figure 4.3). During the second stage, the values lie between -11.8 and 13.2 degrees. On the final stage of the experiment, the horizontal rotation values range between -25.3 and 28.2 degrees. Like the vertical rotation, the horizontal rotation histograms took the shape of normal distributions. Taking the absolute values of all the rotations, the cumulative horizontal rotation values reach up to 60 degrees.

4.2.3 Local Strains

Studying the local strains distributions in Figures 4.4, 4.5 and Appendix B (Figures B1 to B4), a considerable similarity can be noticed between the lateral strains (ε_x and ε_y) throughout the experiment. They always had a Log-Normal distribution that tends to have more positive values then negative. The positive sign here indicates dilation, or expansion, and that's what is expected to happen during the compression of the specimen, where it expands laterally. During the last stage of the experiment, it is noted that there is some difference in the shape of the lateral strains histograms. This happens because the bulging at failure in the middle portion of the specimen (where the CT scans are taken) is not perfectly symmetric around the z axis. The specimen might expand laterally in one direction more than the other, but there is an overall similarity between the lateral stain values, due to the axisymmetry.

On the other hand, the axial strain (ε_z) distributions take a normal distribution shape in the first and second stages of the experiment, the distributions always have a negative mean that indicates compression, and this is the expected result when axially compressing a specimen. On the final stage, the negative values dominate, resulting in a Logistic distribution where most of the values lie in the negative (compression) area. This result indicates the higher values in axial strains obtained at failure.

All the local shear strains histograms took the shape of a Logistic distribution. The positive or negative signals for the shear strains only indicate the direction of shearing, and are not related to the expansion or compression. In the first stage of the experiment 90% of the values of the horizontal shear strains (ε_{xy}) range between -0.104 and 0.111, while in the second stage they lie between -0.133 and 0.150. An as seen in the axial and lateral stains as well as the translation, the greatest increase is noted in the last stage of the experiment, where 90% of the

data is between -0.401 and 0.472. The other shear strains (ε_{xz} and ε_{yz}) distributions also shows a similarity that is caused by the axisymmetric conditions. Both of them have 90% of the values between -0.1 and ~0.1 in the first stage of the experiment. In the second stage, the values range between -0.152 and 0.136 for ε_{xz}, and -0.143 and 0.156 for ε_{yz}. As expected, the larger increase takes place in the last stage of the experiment, where the values of ε_{xz} range between -0.429 and 0.398, and the values of ε_{xz} lie between -0.429 and 0.435.

The rotation strain histograms also took the shape of logistic distributions (Table 4.6). The similarity of the rotation strain distributions throughout the specimen, specially the rotation strains that have a vertical component (ω_{xz}, ω_{yz}). During the first compression stage, (global ε_z = 7.8%), the 90% confidence interval lies between -0.121 and 0.109 for ω_{xy}, -0.094 and 0.083 for ω_{xz}, and -0.092 and 0.100 for ω_{yz} (Figure 4.5). The values of the rotation strains increased during the second compression stage, where 90% of the rotation strains values ranges between –0.193 and 0.152 for ω_{xy}, -0.173 and 0.123 for ω_{xz}, and -0.177 and 0.202 for ω_{yz} (Figure B3). Like all the other strain components, the largest increase in the rotation strains took place in the last stage of the experiment. ω_{xy} had a 90% confidence interval between -0.419 and 0.342. ω_{xz} and ω_{yz} had 90% confidence intervals of -0.540 to 0.433, and -0.431 to 0.438, respectively (Figure B4).

4.2.4 Dilatancy Angles

The dilatancy angles in the first level of compression took a wide range of values, between -41.9 and 70.8 degrees (Figure 4.6 and Table 4.7), where the negative sign indicates contraction whereas positive sign indicates dilation. In this stage of the test some contraction took place in the specimen, and then dilation started (Figure 3.7), it can be realized that the dilatancy angles at this level had more positive values than negative. As the dilation of the

specimen continues at the later levels of the experiment, the fraction of positive dilatancy angles gradually increases, where at the final stage of the test, positive values dominate the dilatancy angle distribution, and a smaller range of dilatancy angle values were obtained (-12.6 to 65 degrees).

CHAPTER FIVE

SPATIAL POROSITY DISTRIBUTION OF ROCK CORES STUDIED BY μCT

5.1 INTRODUCTION

In this part of the thesis, CT technology was used to study the porosity distribution of synthetic rock cores. Several rock cores having different grain size distributions, and prepared under different consolidation pressures were scanned. A density calibration to correlate the CT number to the bulk density was conducted, and then the correlation was used to obtain the porosity distribution for the cores. They were compared to determine the effect of grain size distribution and consolidation pressure on the local porosity distribution of the cores.

5.2 EXPERIMENTAL WORK

5.2.1 Specimen Description

Twelve synthetic rock cores were used in this study. The cores were prepared by mixing Quartz (SiO_2) with four classes (Powder, 0.126-0.149 mm, 0.149-0.177 mm, and 0.177-0.210 mm) and consolidating (Compacting) them under 3000, 4000 or 5000 psi pressures. The main constituent of the cores is the Quartz powder. The cores were prepared by thoroughly mixing the particles and adding liquid glass as a cementing agent. Table 5.1 shows a list of the cores along with their grain size distribution, and the compaction pressure used to prepare them. The cores have a cylindrical shape, with an average radius of 28 mm and an average height of 29 mm (Figure 5.1).

Table 5.1: Rock cores list

Core Name	Consolidation Pressure [psi]	Grain Size [%]			
		Quartz flour	0.126 - 0.149 mm	0.149 - 0.177 mm	0.177 - 0.210 mm
3k_100	3000	100	0	0	0
4k_100	4000	100	0	0	0
5k_100	5000	100	0	0	0
3k_80	3000	80	6	6	8
4k_80	4000	80	6	6	8
5k_80	5000	80	6	6	8
3k_60	3000	60	12	12	16
4k_60	4000	60	12	12	16
5k_60	5000	60	12	12	16
3k_40	3000	40	18	18	24
4k_40	4000	40	18	18	24
5k_40	5000	40	18	18	24

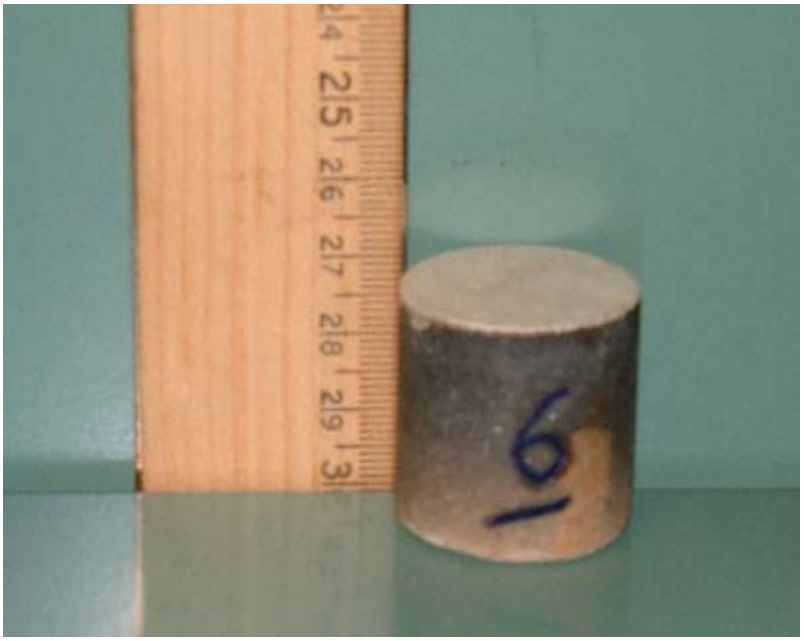

Figure 5.1: A Sample Core

5.2.2 CT Scanning

The CT scans were performed using the Washington State University CT laboratory in August, 2003, using a system similar to the MSFC CT system (Figure 5.2), with a different x-ray source. The x-ray was generated using an X-tek 225 kV microfocus x-ray source (Figure 5.3). It has a 5 μm focal spot size x-ray source with microfocus option that can produce an intense x-ray beam with minimum penumbra. It took approximately 6 minutes to scan each specimen at energy level of 142 keV and 0.158 mA current. The distances from the x-ray source to the specimen and from the specimen to the detector panel were 244.5 and 416 mm, respectively, producing about 700 slices per core. Each slice is about 620 x 620 pixels yielding a spatial resolution of about 47.83 μm/pixel. Figure 5.4 shows example CT renderings of one of the scanned cores.

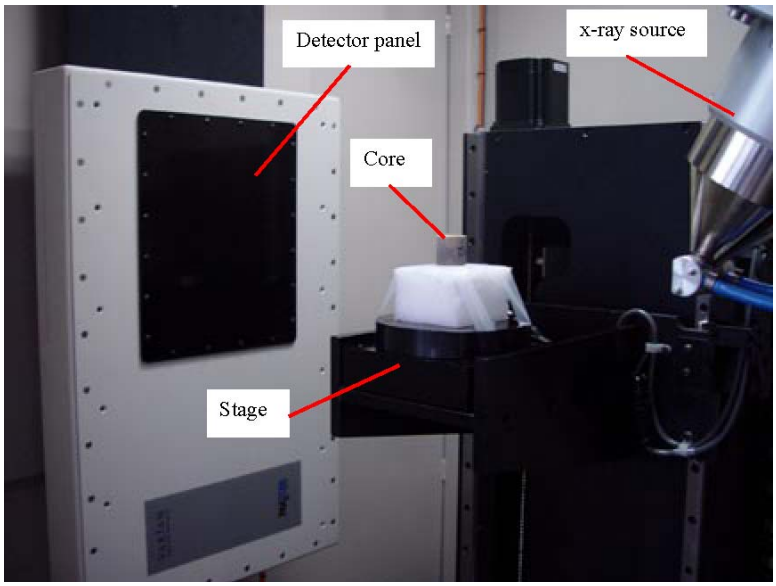

Figure 5.2. The X-ray CT System of Washington State University (WAX-CT)

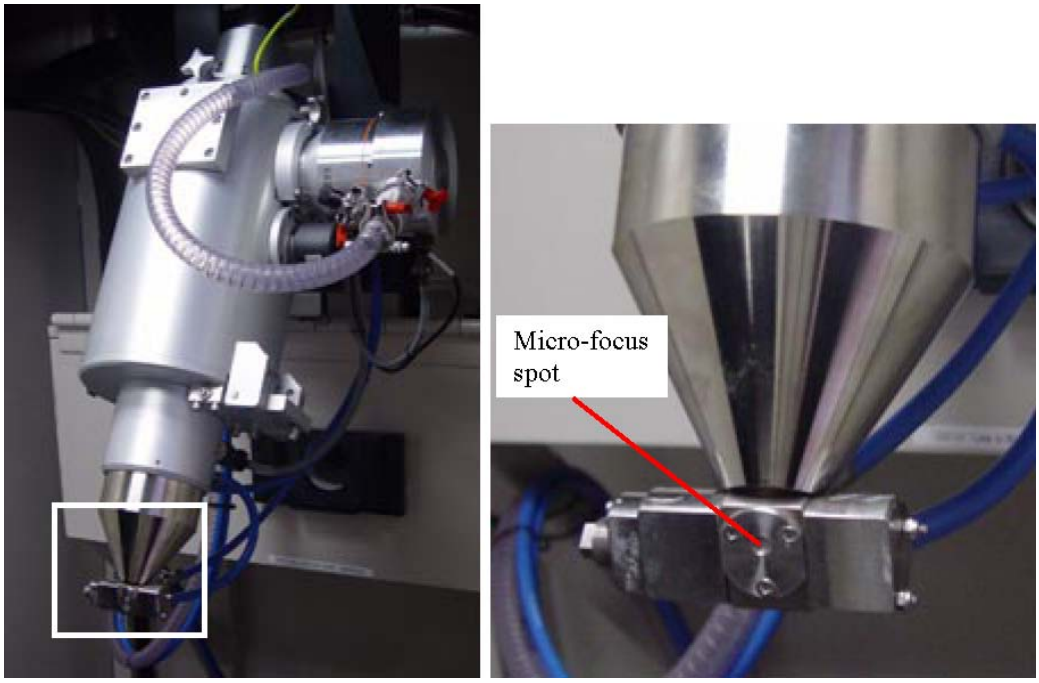

Figure 5.3. The X-tek 225 kV Microfocus x-ray source

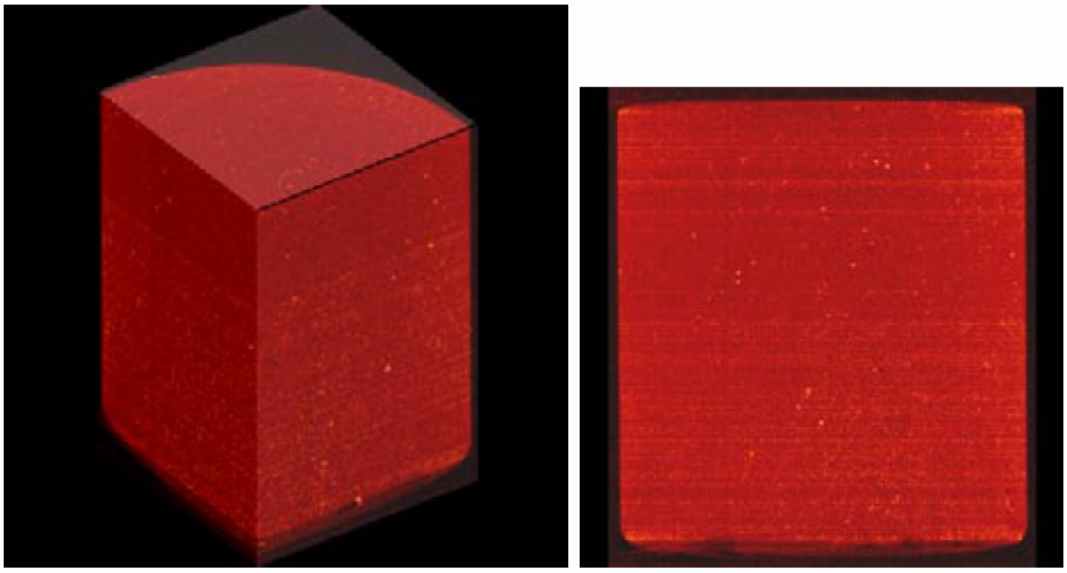

Figure 5.4. Example wedge view and axial CT sections of a core

5.3 POROSITY CALCULATIONS

5.3.1 Density Calibration

Density calibration was performed using the ASTM guidelines (ASTM E1935, 1997). Three materials were used to perform the calibration: Aluminum, Graphite, and Acrylic. The densities (ρ) of the materials were calculated through weight and volume measurements, and the mass attenuation coefficients (MCA) were obtained from the NIST website (Hubbell and Seltzer, 1997). Then the linear attenuation (Ca) was calculated as the product of the density and the mass attenuation (Equation 5.1). The scanning was performed at the same energy and geometric settings as the cores. The mass attenuation coefficients, densities and the average CT numbers for the calibration materials are shown in Table 5.2, and the density calibration curve is shown in Figure 5.5.

$CA\ (cm^{-1}) = \rho\ (gm/cm^3) * MCA\ (cm^2/gm)$ …… (5.1)

The correlation in Figure 5.5 was then used to calculate the bulk density of the rock cores. The mass coefficient of attenuation (MCA) of quartz was calculated at 142 keV as 0.1447 (cm^2/g), and then from the CTN data using the correlation in Figure 5.5 the bulk density can be calculated from Equation 5.1 after rearranging the terms. Then the porosity (n) can be calculated using in Equation 2.5.

Table 5.2: The Density Calibration Data.

Material	Mass Attenuation (μCA) (cm^2/g)	Density (ρ) (g/cm^3)	Linear Attenuation (Ca) (cm^{-1})	CTN
Aluminum	0.1434	2.66	0.3814	7840
Graphite	0.1374	1.76	0.2421	4028
Acrylic	0.1425	1.2	0.1710	2046

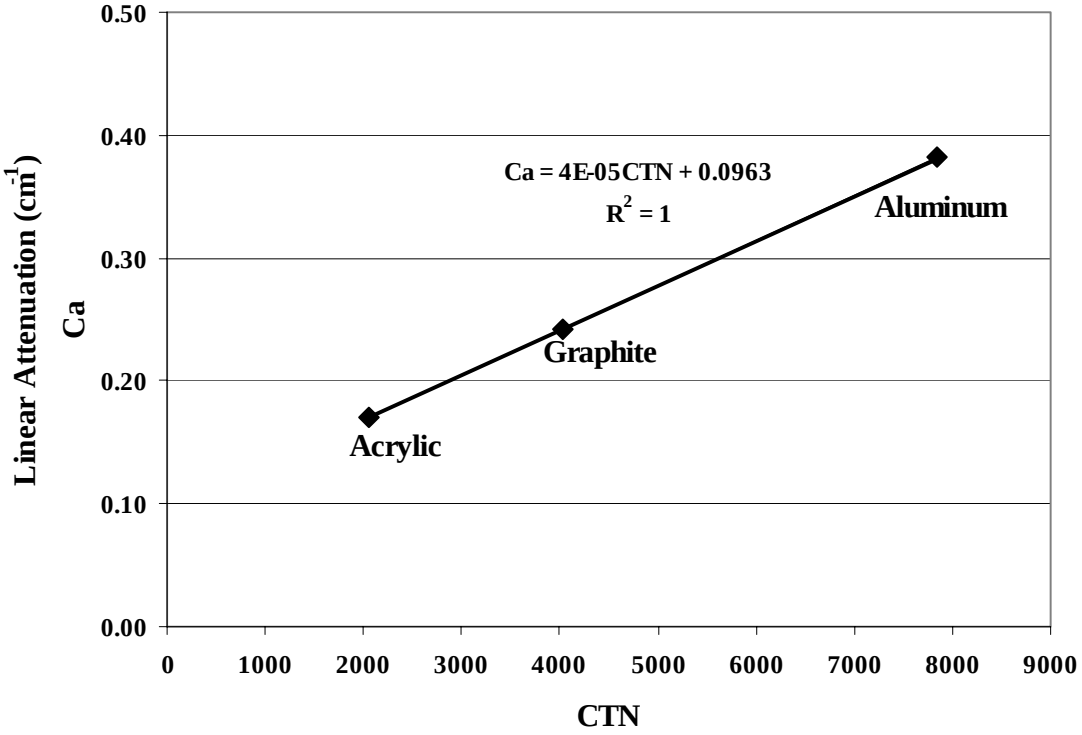

Figure 5.5. The density calibration curve

After subtracting the edges, the 3D data array obtained by stacking the cross sectional slices for each core has the size of approximately (350x350x550) voxels. A computer program was written using the Interactive Data Language (IDL) to calculate the local porosity distribution for each core. The porosity is calculated for small volumes of five voxels, yielding about 15 million n values for each core. Histograms of the local porosity distribution for each core are prepared in order to be able to compare the local porosity distribution for all the cores. And to demonstrate the effect of using different grain size distributions and compactions pressures on the local porosity distribution.

5.4 RESULTS AND DISCUSSION

5.4.1 Effect of Grain Size Distribution

The local porosity histograms for the cores, grouped by the compaction pressure, are shown in Figures 5.6 through 5.8. For each compaction pressure, four cores having different grain size distributions are analyzed, where the percentage of the quartz powder is reduced each time, and different grain size distributions are used.

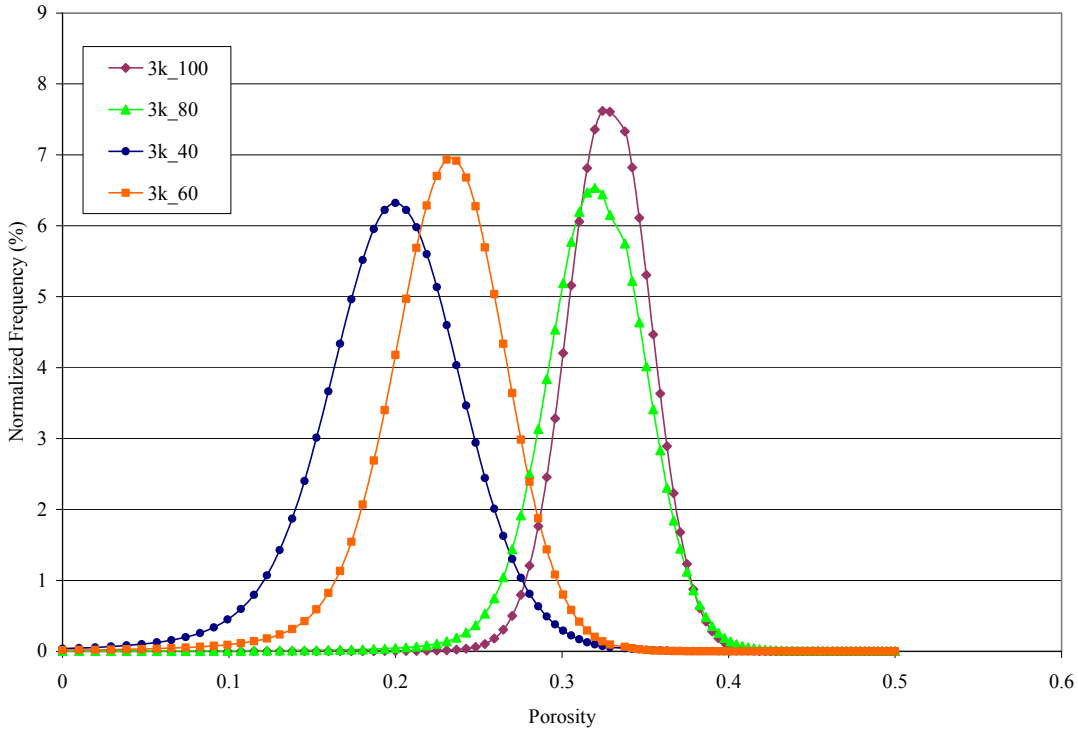

Figure 5.6. Porosity Histograms for 3000 psi Cores

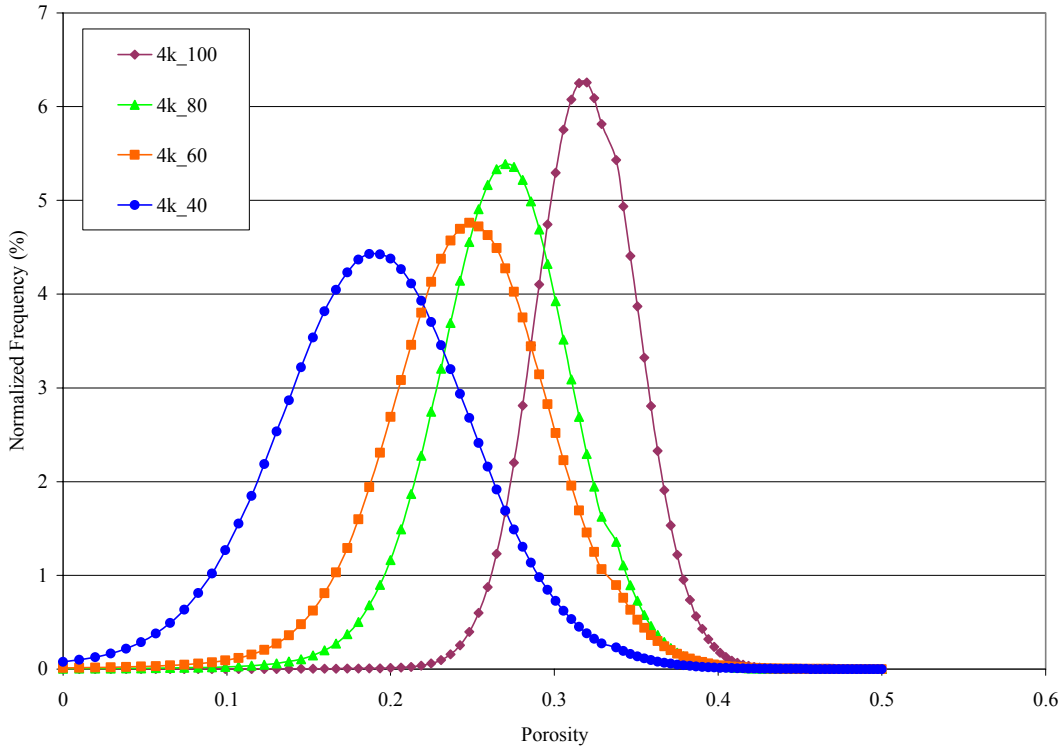

Figure 5.7. Porosity Histograms for 4000 psi Cores

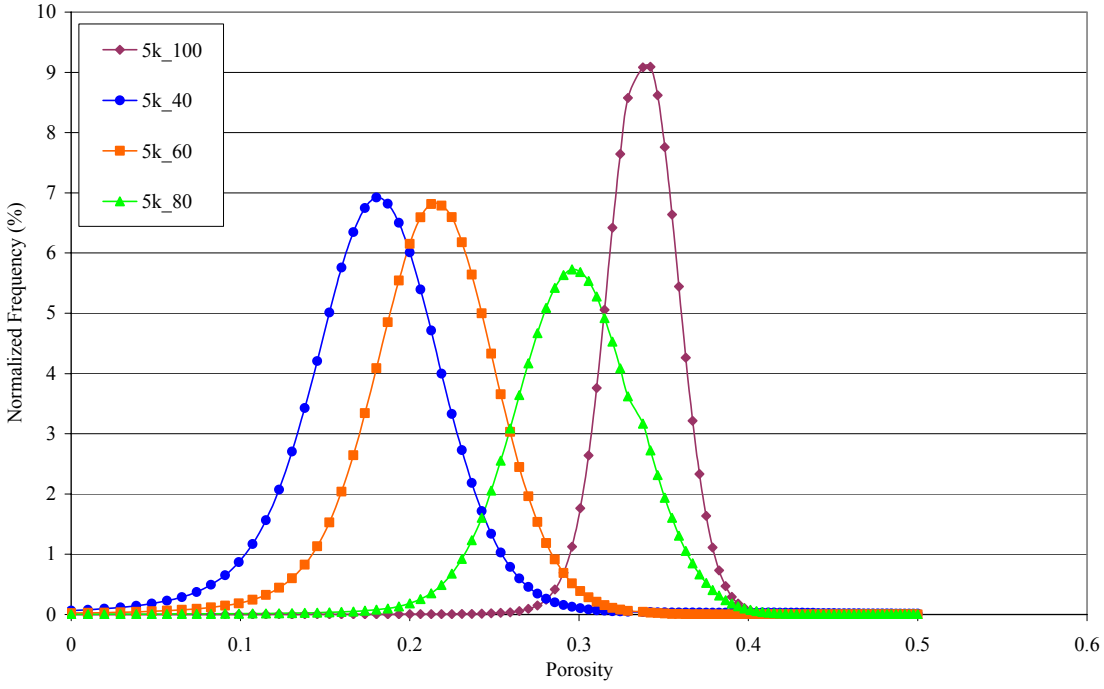

Figure 5.8. Porosity Histograms for 5000 psi Cores

As seen from the histograms, increasing the non uniformity of particles sorting reduces the average porosity of the cores, and this is a well know fact, since providing different sizes of grains helps in filling the small and large voids with the different sizes of particles, resulting in better packing of the particles. To clearly illustrate this concept Figure 5.9(a) shows a poorly graded packing, while Figure 5.9(b) shows a well graded packing. It can be seen that having different particle sizes helps in filling most of the voids, resulting in a lower porosity value.

.

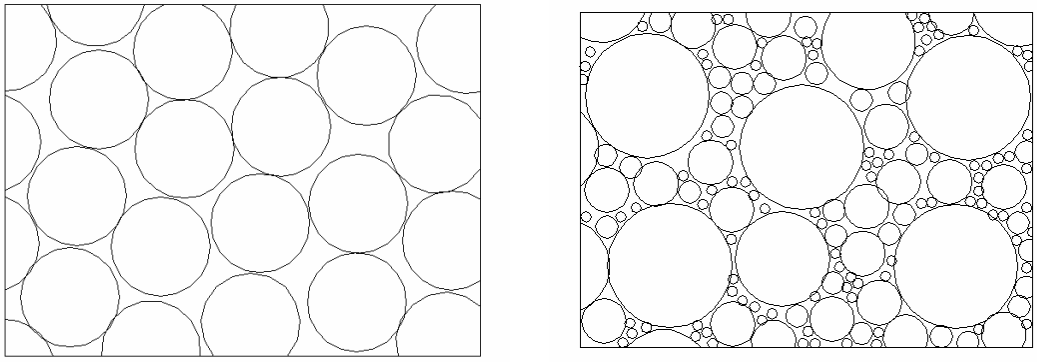

(a) (b)

Figure 5.9. (a) A poorly graded packing. (b) A well graded packing

Furthermore, the shapes of the histograms tend to be wider (i.e. higher standard deviation) with increasing the grain size distribution, where a wider porosity histogram indicates a lager variety of void sizes within the core. If the core has one grain size, it has nearly same pore size, so, if we look into a small volume (five voxels in our case) we will find that it will have nearly the same percentage of pores and solids, therefore, we can say that it is a homogeneous medium, and that results in the "narrow" histograms for the 100% powder cores. Figure 5.10a shows three random areas selected in a homogeneous medium. It can be seen that all the areas

contain nearly the same proportions of solid and void areas. On the other hand, looking at a core having a variety of grain sizes, it will have different pore sizes, resulting from the different sizes of the particles. Therefore, considering a small volume (5 voxels) in different positions, will yield in a wide variety of void to solid ratios (Figure 5.10b), resulting in a high standard deviation value and wider porosity histograms. A summary of the means and standard deviations of the local porosity histograms is shown in Table 5.3.

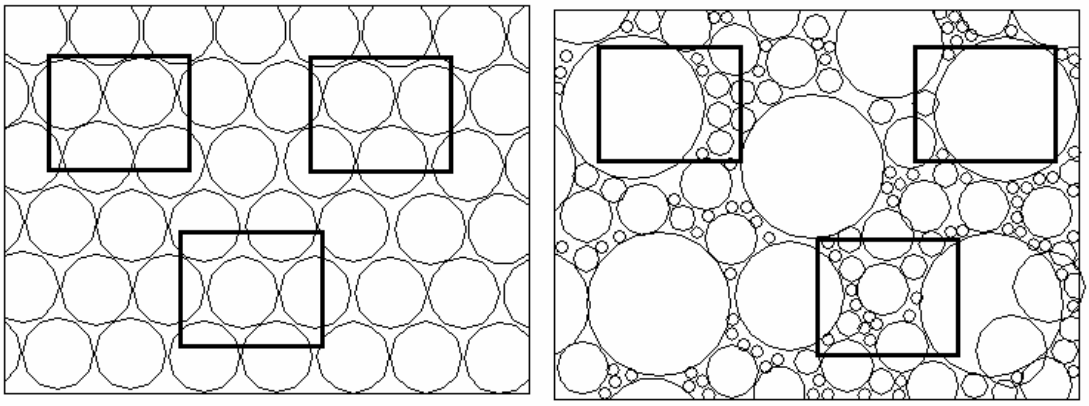

(a) (b)

Figure 5.10. (a) Selection of a random area in a poorly graded specimen (b) selection of a random area in a well graded specimen.

Table 5.3: Summary of the statistical parameters for the porosity distributions

Core	Mean	Std. Dev.	Variance	Skewness	Kurtosis
3k_100	0.331951	0.0243841	0.0005946	-0.677971	9.15775
4k_100	0.324608	0.0307659	0.0009465	-0.742309	12.1766
5k_100	0.340829	0.0218543	0.0004776	0.387745	38.6906
3k_80	0.324644	0.031345	0.0009825	-1.16835	13.1452
4k_80	0.276654	0.0419643	0.001761	-0.67183	5.63001
5k_100	0.303162	0.0370358	0.0013717	-0.805755	5.93213
3k_60	0.237291	0.0385848	0.0014888	-1.47545	12.0596
4k_60	0.257841	0.0506909	0.0025696	-0.630058	5.4647
5k_60	0.220352	0.0413722	0.0017117	-1.286	10.4692
3k_40	0.206179	0.046165	0.0021312	-0.997361	7.97292
4k_40	0.20234	0.0628318	0.0039478	-0.630799	6.53747
5k_40	0.199239	0.0426337	0.0018176	-1.38796	10.8378

5.4.2 Effect of Compaction Pressure

The cores are grouped into four groups. The cores in each group have the same grain size distribution, but each core was prepared at a different compaction pressure. The porosity histograms for the four groups are shown in Figures 5.11 through 5.14.

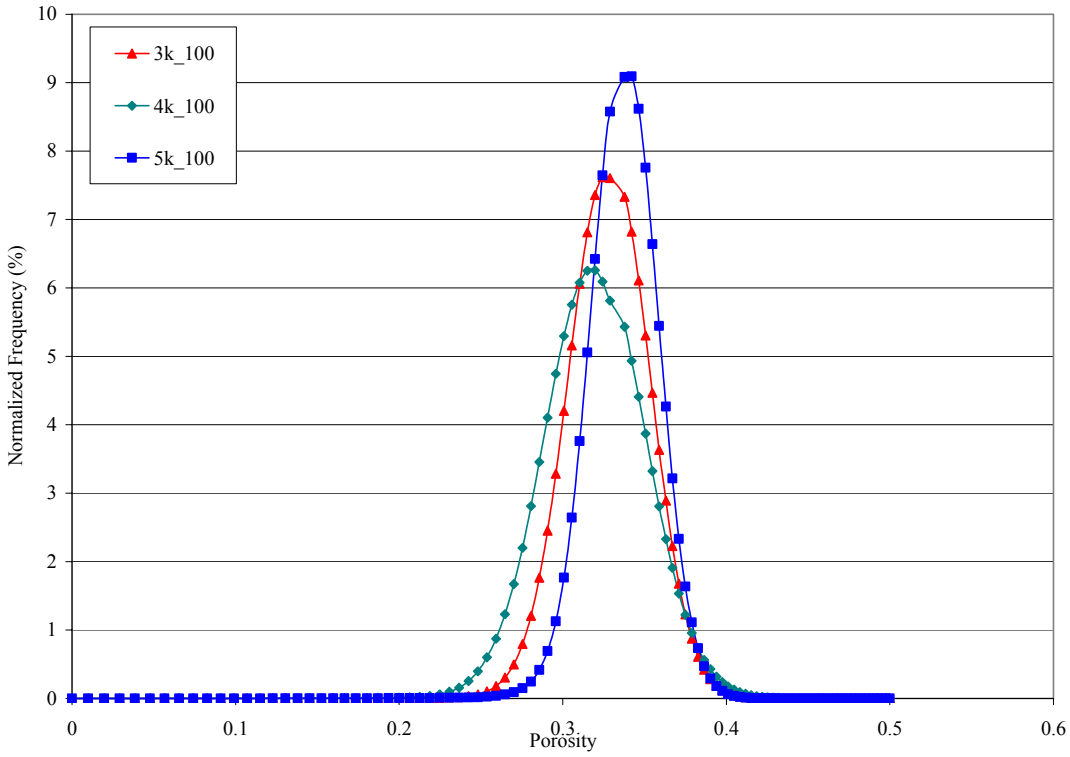

Figure 5.11. Porosity Histograms for 100% Quartz Powder Cores

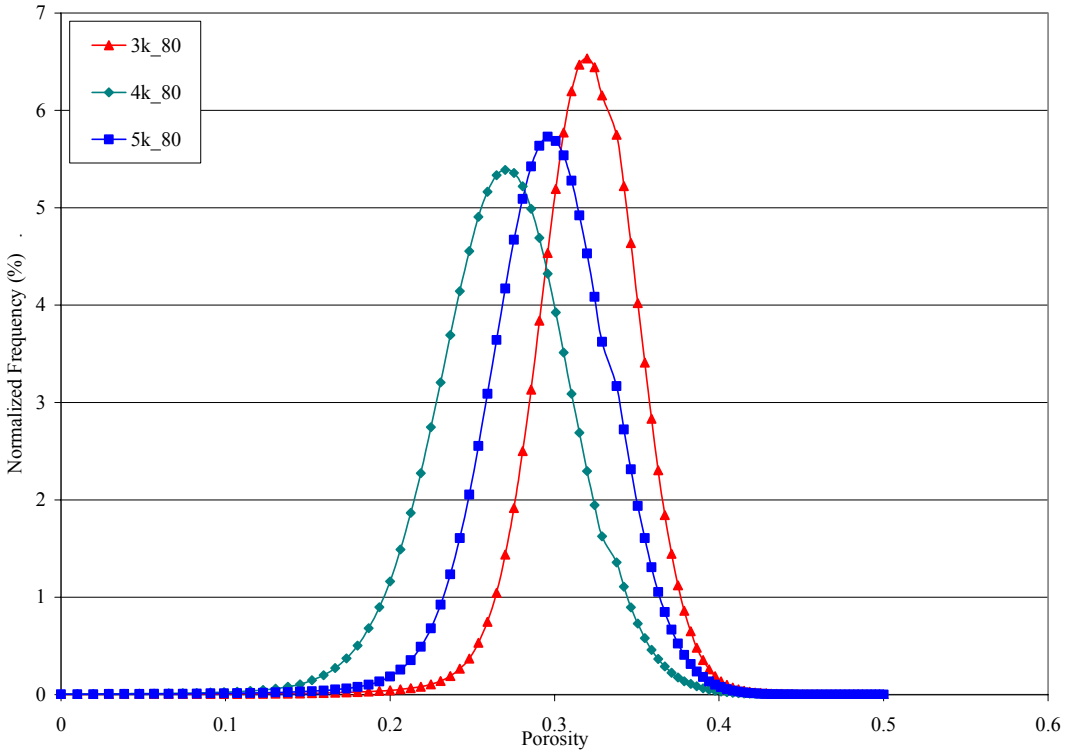

Figure 5.12. Porosity Histograms for 80% Quartz Powder Cores

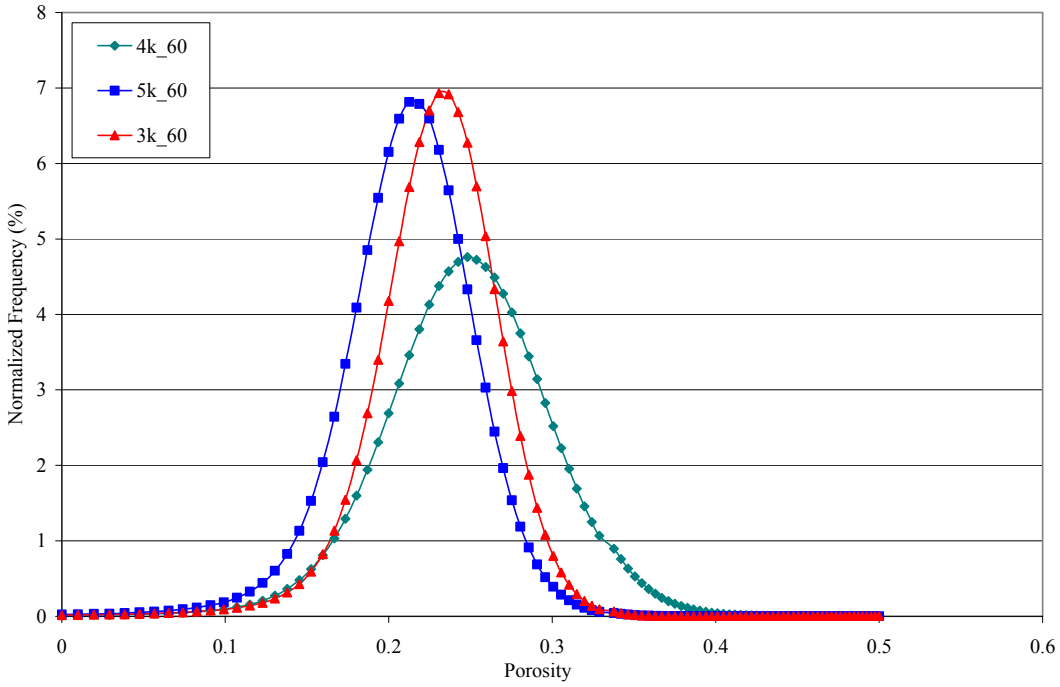

Figure 5.13. Porosity Histograms for 60% Quartz Powder Cores

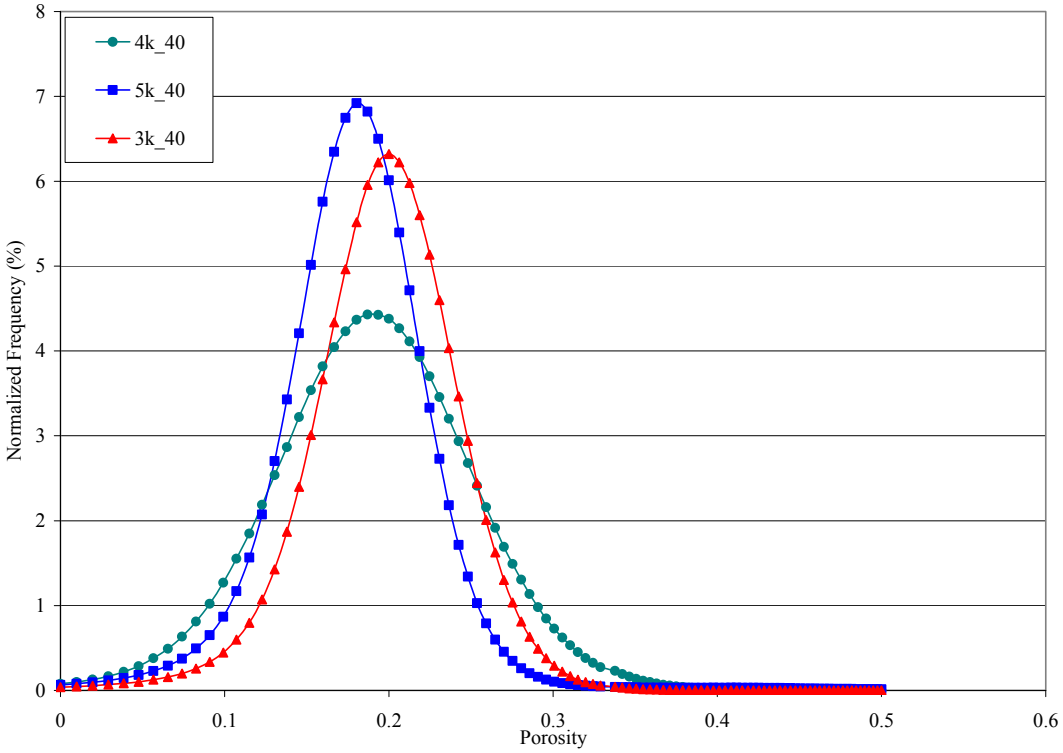

Figure 5.14. Porosity Histograms for 40% Quartz Powder Cores

It is expected that increasing the compaction pressure, should decrease the porosity of the cores. This was not the case for the cores under investigation. Increasing the compaction pressure from 3000 psi to 4000 psi resulted in decreasing the porosity as expected. But on the other hand, increasing the compaction pressure to 5000 psi did not reduce the porosity. The porosity histograms for the 5000 psi cores were located and different location each time with respect to the 3000 and 4000 psi cores histograms (Figures 5.11 – 5.14). This may be due to the crushing of the particles that occurred at the very high pressure that resulted in the irregularity of the particles` shapes, resulting in the unexpected values for the porosity. Moreover, large particles are more susceptible to crushing than smaller ones, and it can be seen in the cores having a

higher percentage of large particles (40% and 60% Quartz powder) experience an irregularity of results that can be justified by the crushing of the large (0.177 - 0.210 mm) particles at lower compaction pressures of 4000 or even 3000 psi. It can also be realized that the porosity values for the cores having the same grain size distribution, and different consolidation pressures are very close to each other, because the lowest consolidation pressure used (3000 psi) is already a very high pressure, and it might be enough to achieve the highest possible compaction for the particles, and not much more compaction can be achieved by increasing the consolidation pressure. As a result of the closeness of the porosity values for these cores, any imperfections in the preparation process or the measurement could result in misleading trends in the results. This could be another reason for the irregularity of the results for those cores.

5.4.3 Vertical Profiles of Porosity

To demonstrate the variation of porosity along the height of the cores, the average porosity values for each slice were calculated for every core, and plotted against the distance from the bottom of the core (Figure 15.15). All the profiles followed the same trend, where the porosity increases near the ends, and decreases near the middle of the cores, this could be due the boundary conditions of the cores where the edges doesn't get as compacted as the middle part of the cores.

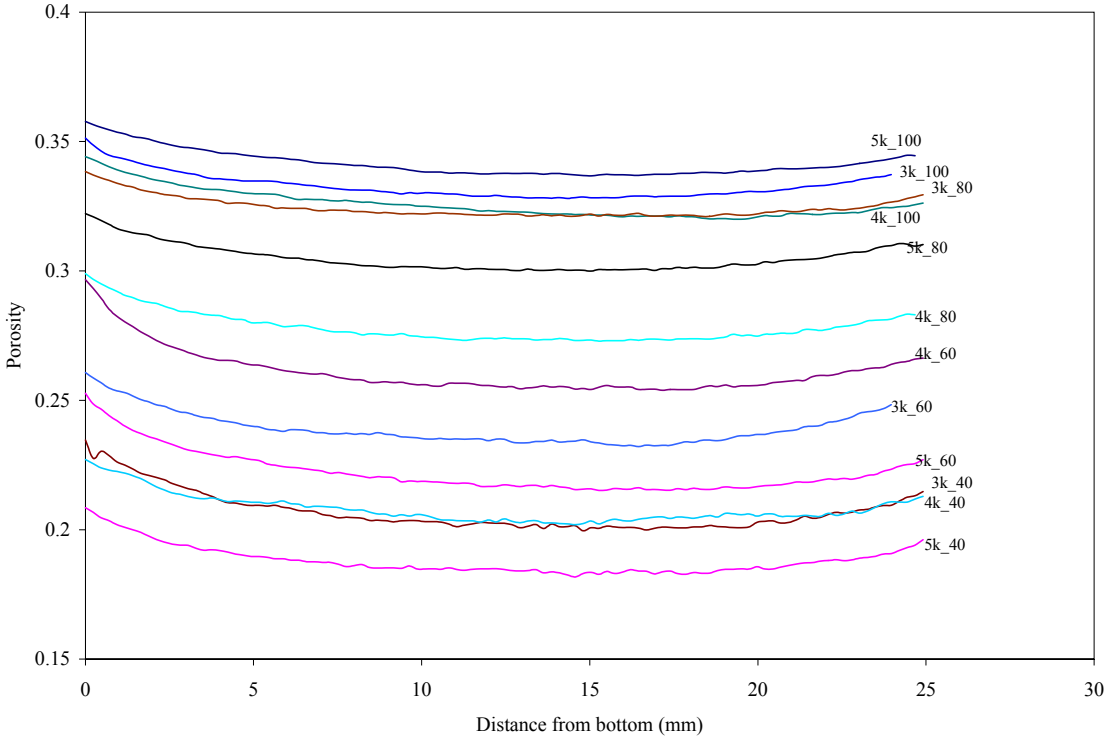

Figure 15.15. Vertical profiles of the porosity distributions of the rock cores.

CHAPTER SIX

CONCLUSIONS AND RECOMMENDATIONS

6.1 CONCLUSIONS

This thesis has two objectives. The first is to use micro-focus computed tomography (μCT) to study the shearing of granular materials, and the second is to characterize the variation of the local porosity distributions of synthetic rock cores with changing the grain size distribution and consolidation pressure using μCT. To achieve the first objective a triaxial specimen was scanned at different strain levels to track the translation and rotation of the particles within the specimen. The obtained values for translation and rotation were used to calculate the local strain distribution within the specimen, and the distributions were compared to study the behavior of the particles at different stages. To achieve the second objective, twelve different rock cores were scanned. The cores were prepared at different compaction pressures, and have different grain size distributions. Density calibration was performed to correlate the CT numbers to the bulk density and porosity. Local porosity distributions of the cores were obtained using this correlation. They were porosity compared to find the effect of compaction pressure and grain size distribution.

Using the 3D volumetric data obtained by CT, the values of translation and rotation of the particles in the triaxial specimen were obtained at a high degree of precision, for all stages of the compression. This data was used to calculate the local strain distribution of the specimen throughout the test. The calculated local strains were increasing throughout the experiment, especially in the last stage, were a large increase in the local strains values was noticed. It was also realized the local strains in the radial directions (ε_x and ε_y) showed a similarity throughout

the test, where all the histograms took the shape of a Log-Normal distribution, with a greater number of positive (extension) values then negative (contraction) values. This is due to the axisymmetric conditions of the test. All the local shear strain histograms took the shape of a logistic distribution; their values in the first two stages of the experiment lied in the narrow range of ± 10% to 15%. On the last stage of compression a large increase in the shear strains values increased to reach up to ± 40%.

A similar trend was noticed in the rotation strain values, where all the histograms had the shape of a logistic distribution. During the first and second stages of compression the rotation strain values had values within ± 20%. They increased to reach about ±50% during the final stage. A wide range of values was noticed for the dilatancy angles. At the beginning of the test, the values where nearly evenly distributed between positive (dilatancy) and negative (contraction). At the later stages, more positive values where obtained due to the dilative nature of the specimen, until the last stage of the experiment where the positive values where dominant.

On the other hand, μCT showed an excellent ability to track the changes in the local porosity distribution, and the homogeneity of pore sizes of the of the synthetic rock cores. It was found that when using well graded grains less porosity values and inhomogeneous pore sizes were obtained, while when using poorly graded grains, higher porosity values and homogeneous pore sizes were obtained, this was obtained from the mean and standard deviations of the porosity distributions of the cores. No clear trend was obtained when increasing the consolidation pressure. This could be due to the crushing of the particles at the very high consolidation pressures, and some imperfections in the preparation process of the rock cores, which resulted in inconsistent results for the porosity distribution.

6.2 RECOMMENDATIONS

- The data presented in the first part of this thesis could be compared with the values obtained from different theoretical models. This could help in improving modeling of the constitutive behavior of granular materials.
- In this study, plastic beads where used to model the behavior of granular materials. The possibility of using other materials, like sand, should be investigated. This requires the improvement of the CT scanner resolution, and the development of computer programs to identify the particles and track their translation and rotation.
- In order to be able to relate the local values of strains and dilatancy angles to the global values, the whole specimen should be scanned. This will require a larger scanning times, and data sizes. It will also require very high computer capabilities and storage space. So, in order to achieve this goal all these requirements should be considered.
- Further studies should be conducted on the effect of increasing the consolidation pressure on the porosity distribution of rock cores. A wider range of consolidation pressures should be considered, with special care taken in the preparation process, to reduce the amount of error caused my imperfections in the preparation of the cores.

REFERENCES

Alfaro M.C. and Wong, R.C.K. (2001): Some Applications of Computerized Tomography (CT) Scan in Experimental Geotechnics, Proc. 15th International Conference in Soil Mechanics and Geotechnical Engineering , Istanbul, Turkey, 2001, Vol. 1, pp. 337-342

Alshibli, K.A., Batiste, S.N., Swanson, R.A., Sture, S., Costes, N.C., Lankton, M.R., (2000a): Quantifying Void Ratio Variation in Sand Using Computed Tomography, Geotechnical Measurements: Lab and Field, Proceedings of the sessions of Geo-Denver 2000, Denver, Colorado, August 5-8, 2000.

Alshibli, K.A., Sture, S., Costes, N.C., Frank, M.L., Lankton, M.R., Batiste, S.N., Swanson, R.A., (2000b). Assessment of Localized Deformations in Sand Using X-Ray Computed Tomography, Journal of Geotechnical Testing, 23(3):274-299.

Alshibli, K.A., (2004): Unpublished Work

Amersham Health, (2004): Encyclopaedia of Medical Imaging by NICER (Medycyclopedia) online version, http://www.amershamhealth.com/medcyclopaedia/.

Anandarajah, A., (2004): Sliding and Rolling Constitutive Theory for Granular Materials, Journal of Engineering Mechanics, Vol. 130, No. 6, June, 2004.

Bansal, A., Islam, M. R., (1991): State-of-the-Art Review of Nondestructive Testing with Computer-Assisted Tomography, SPE 22127, International Arctic Technology Conference, SPE, Anchorage, Alaska, May 29-31, 1991.

Bossi, R.H., Friddel, K.D., Lowery, A.R., (1990): Computed Tomography. Non-Destructive Testing of Fiber-Reinforced Plastic Composites, New York, Elsevier Applied Science.

Barrington Medical Imaging LLC Website, 2004, http://www.bmimed.com/ct-imaging.asp.

Cromwell, V., Kortum, D.J., Bradely, D.J., (1984): The Use of a Medical Computer Tomography (CT) System To Observe Multiphase Flow in Porous Media, SPE 13098, 59th Annual Technical Conference and Exhibition, SPE, Houston, Texas, September 16-19, 1984

Desrues, J., Chambon, R., Mokni, M., Mazerolle, F., (1996): Void Ratio Evolution Inside Shear Bands in Triaxial Sand Specimens Studied by Computed Tomography, Geotechnique 46, No. 3, 529-546.

Frost, J.D., and Jang, D.J., (2000): Evolution of Sand Microstructure During Shear", ASCE, Journal of Geotechnical and Geoenvironmental Engineering, Vol. 126, No.2, pp. 116-130.

Fujii, M., Uyama, K., (2003): Recent Advances on X-ray CT, , Proceedings of the International Workshop on X-ray CT for Geomaterials, Kumamoto, Japan, 6-7 November 2003.

Honarpour, M.M., Cromwell, V., Hatton, D., Satchwell, R., Reservoir Rock (1985): Descriptions Using Computed Tomography (CT), SPE 14272, 60th Technical Conference and Exhibition, SPE, Las Vegas, Nevada, September, 22-25, 1985.

Hubbell, J.H., and Seltzer, S.M., (1996): Tables of X-Ray Mass Attenuation Coefficients and Mass Energy-Absorption Coefficients", NIST web site (http://physics.nist.gov/PhysRefData/XrayMassCoef/cover.html).

K. Kanatani (1979): A micropolar continuum theory for the flow of granular materials, International Journal of Engineering Science, Vol. 17, No. 4 (1979), pp. 419-432

Ketcham, A.R., Carlson, D.W., (2001): Acquisition, and optimization and interpretation of X-ray computed tomographic imagery: Application to the Geosciences, Computer & Geosciences, 27:381-400.

Kropas-Hughes C., Neel, S., (2000): Basics of Computed Tomography. Website of The American Society for Nondestructive Testing (ASNT). http://www.asnt.org/publications/materialseval/basics/may00basics/may00basics.htm

KTH Royal institute of technology (2001): Computed Tomography, November 2001.

Kuhn, M. R., Bagi, K., (2002): Particle Rotations in Granular Materials. 15th ASCE Engineering Mechanics Conference, June 2 – 5, 2002, Columbia University, New York, NY.

Michael, G., (2001): X-ray Computed Tomography, Journal of Physics Education 36**,** 442-451.

Mukunoki, T., Otani, J., Obara, Y., Kaneko, K., (2003): Artifacts of X-ray CT Data in the Analysis of Geomaterial Properties, Proceedings of the International Workshop on X-ray CT for Geomaterials, Kumamoto, Japan, 6-7 November 2003.

Oda, M., Iwashita, K., (edt.), (1999): Introduction to Mechanics of Granular Materials, Balkima, 1999.

Oda, M., Konishi, J., and Nemat-Nasser, S. (1982): Experimental micromechanical evaluation of strength of granular materials: Effects of particle rolling. Mech. of Materials, 1(4), 269–283.

Oda, M., Iwashita, K., Kakiuchi, T., (1997): Importance of Particle Rotation in Mechanics of Granular Materials, Powders & Grains 97, Behringer & Jenkins (edt.), Balkema, pp. 207-210, (1997).

Otani, J., Mukunoki, T., Obara, Y., (2000): Application of X-Ray CT Method for Characterization of Failure in Soils, Soils and Foundations, Vol. 40, No. 2, 111-118.

Rowe, P.W., (1962): The Stress Dilatancy Relation for Static Equilibrium of an Assembly of Particles in Contact. Proceedings of the Royal Society. Vol. 269, Series A, pp 500-527.

Sheats, M.J., (2000): Advanced Data Processing for Volumetric Computed Tomography Data, A Masters Thesis, University of California Davis.

Steude, J.S., and F. Hopkins. (1994): Industrial X-ray computed tomography applied to soil research. Tomography of soil-water-root processes. SSSA Spec. Publ. 36. SSSA, Madison, WI.

Strumas, N., Antonyshyn, O., Yaffe, M. J., Mawdsley, G., Cooper, P., (1995): Computed Tomography Artifacts: An Experimental Investigation of Causative Factors, 49th Annual Meeting of the Canadian Society of Plastic Surgeons, Saskatoon, Saskatchewan, June 1995.

Tatsuoka, F. (1987): Discussion: The Strength and Dilatancy of Sands. Geotechnique, 37(2), 219-226.

Van Geet, M., Lagrou, D., and Swennen, R. (2003): Porosity Measurements of Sedimentary Rocks by Means of Microfocus X-ray Computed Tomography (μCT)," from Mees, F. Swennen, R., Van Geet, M. & Jacobs, P. (edrs), "Applications of X-ray Computed Tomography in the Geosciences", *Geological Society of London, Special Publication*, Vol. 215, pp. 51-60.

Vardoulakis, I., Sulem, J., (1995), Bifurcation Analysis in Geomechanics, Blackie Academic & Professional, Bishopbriggs, Glasgow, 1995.

Wang, L.B., Frost, J.D., and Lai, J.S., (1999): Non-Invasive Measurement of Permanent Strain Field Resulting from Rutting in Asphalt Concrete, Transportation Research Record, No. 1687, pp. 85-94.

Washington State University (2004). X-Ray Computed Tomography Facility WAX-CT (http://www.waxct.wsu.edu/)

Wevers, M., De Meester, P., Swennen, R., (2000): Microfocus X-ray Computer Tomography in Materials Research, Proceeding of the 15th World Conference on Nondesructive Testing, Roma, Italy, 15-21 October 2000.

Withjack, E. M., (1987): Computed Tomography for Rock-Property Determination and Fluid-Flow Visualization. 62nd Annual Technical Conference and Exhibition of the Society of Petroleum Engineers, Dallas, TX, September, 1987.

Wood, D.M. (1990): Soil Behavior and Critical State Soil Mechanics, Cambridge, Cambridge University Press.

Yoshikawa, H., (2004): X-ray Computed Tomography. Website of Inouye Labs, Japan. http://ctlab.bk.tsukuba.ac.jp/~hiroki/blind/x-rayCT.html

APPENDIX A: TRANSLATION AND ROTATION HISTOGRAMS

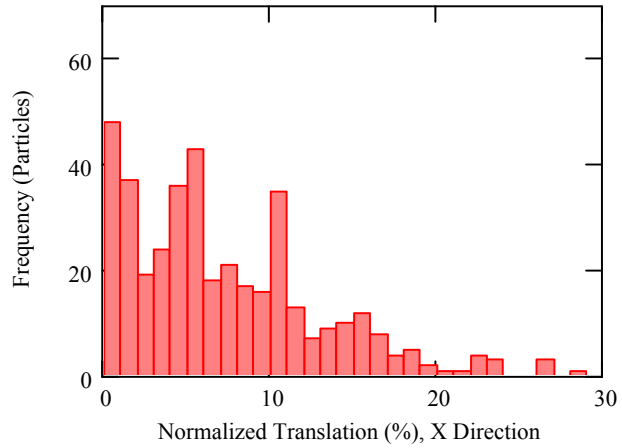

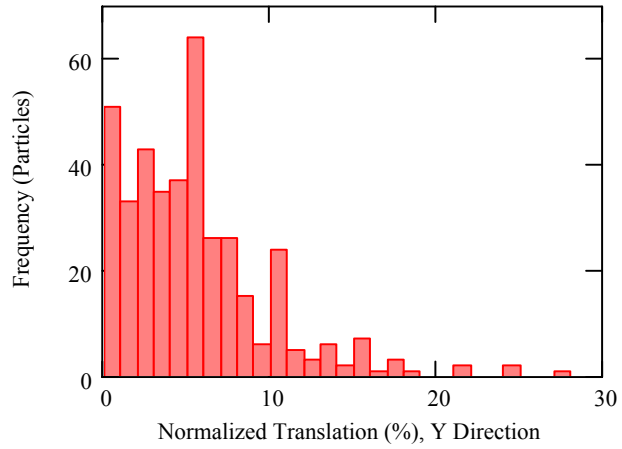

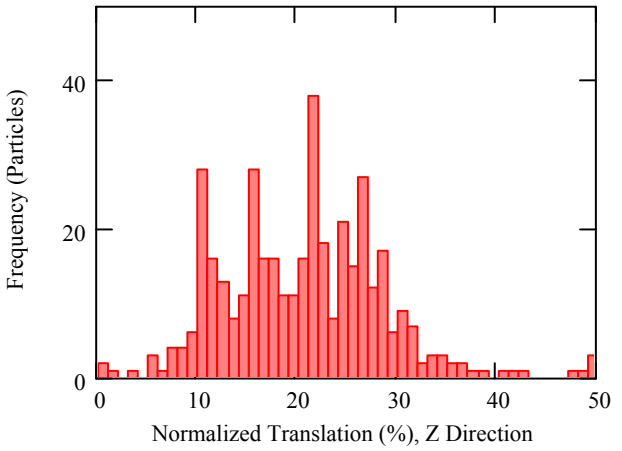

Figure A1: Normalized Translation Histograms at ε_z = -13.7 %
(Normalization Value = 6.6 mm)

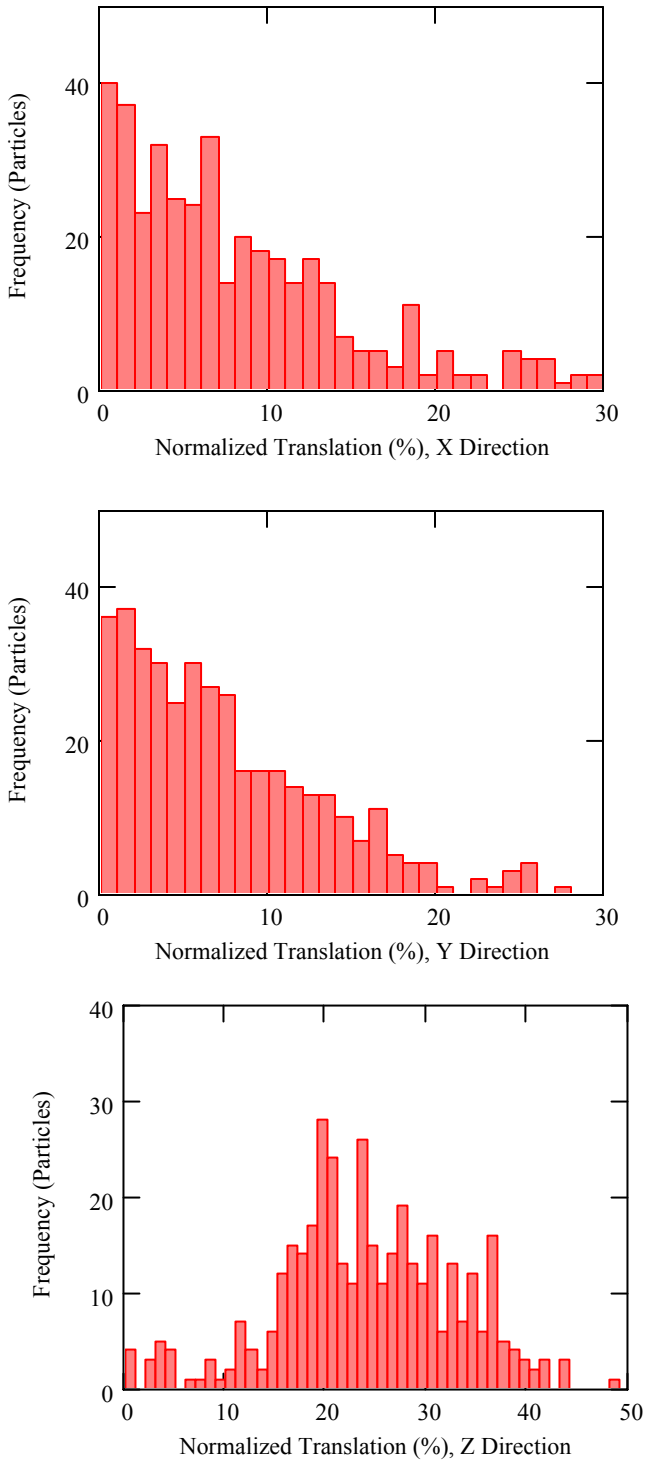

Figure A2: Normalized Translation Histograms at ε_z = -23.5 %
(Normalization Value= 11.4 mm)

APPENDIX B: LOCAL STRAIN HISTOGRAMS

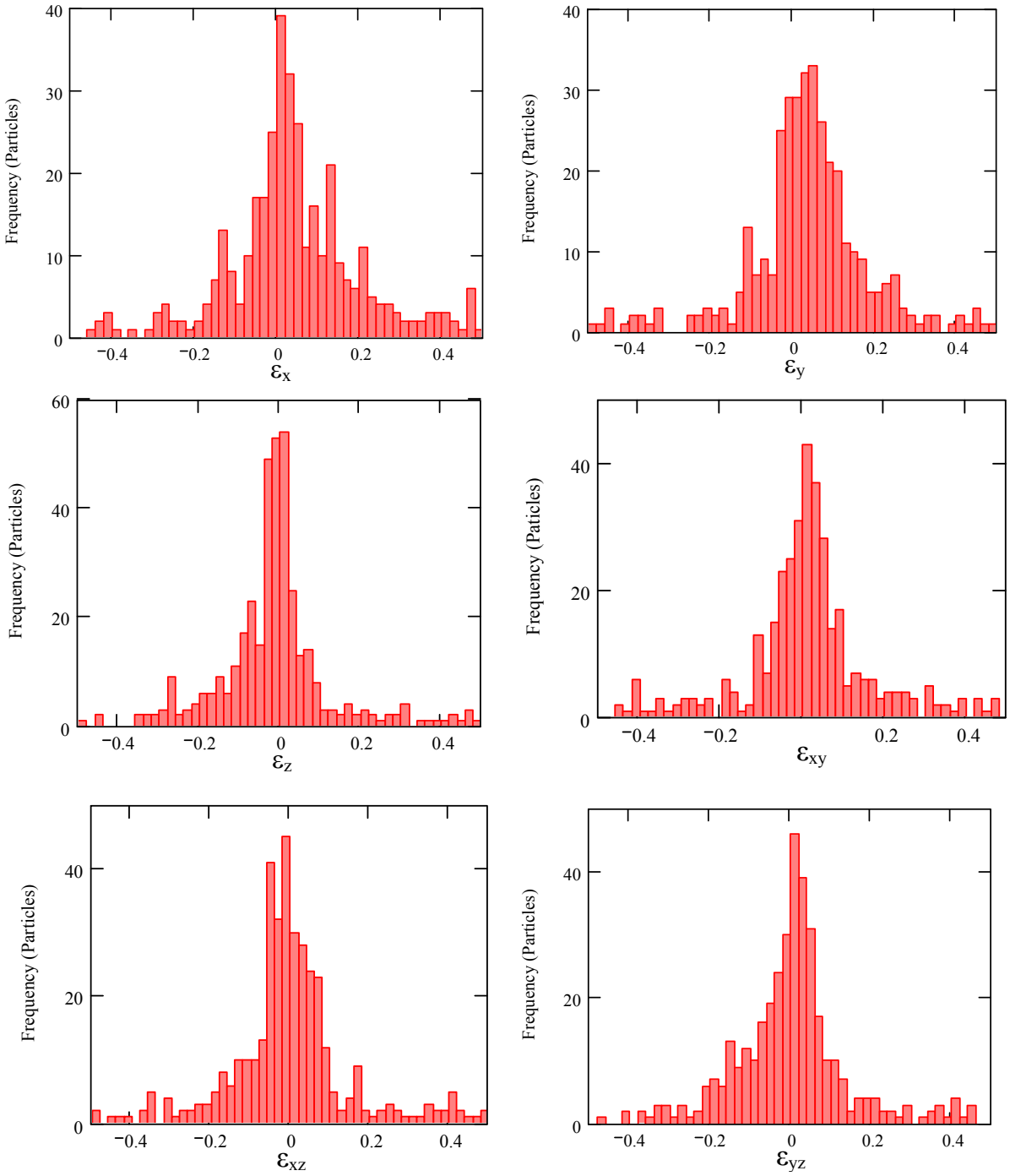

Figure B1: Local strains histograms at ε_z = -13.7%

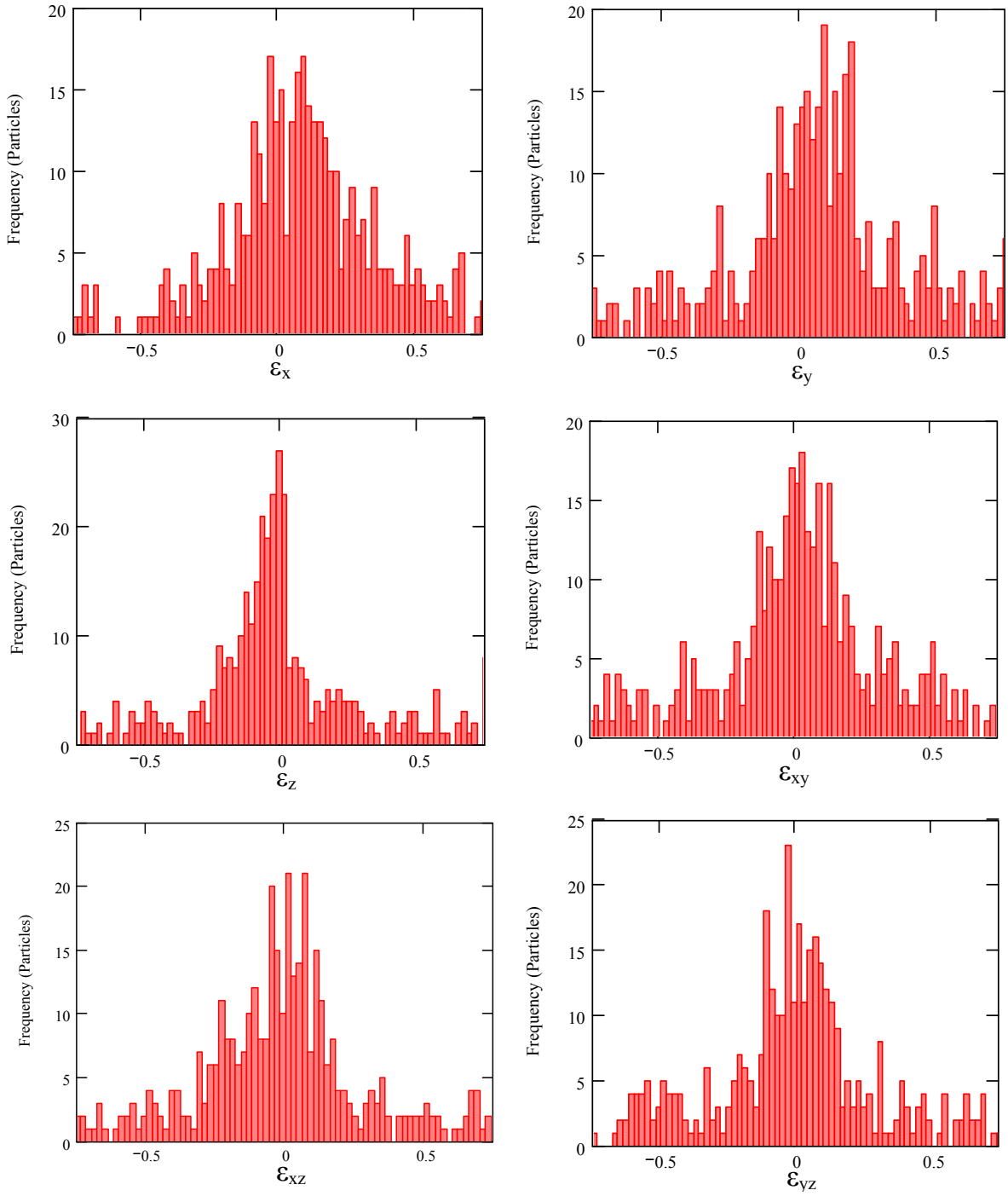

Figure B2: Local strains histograms at ε_z = -23.5%

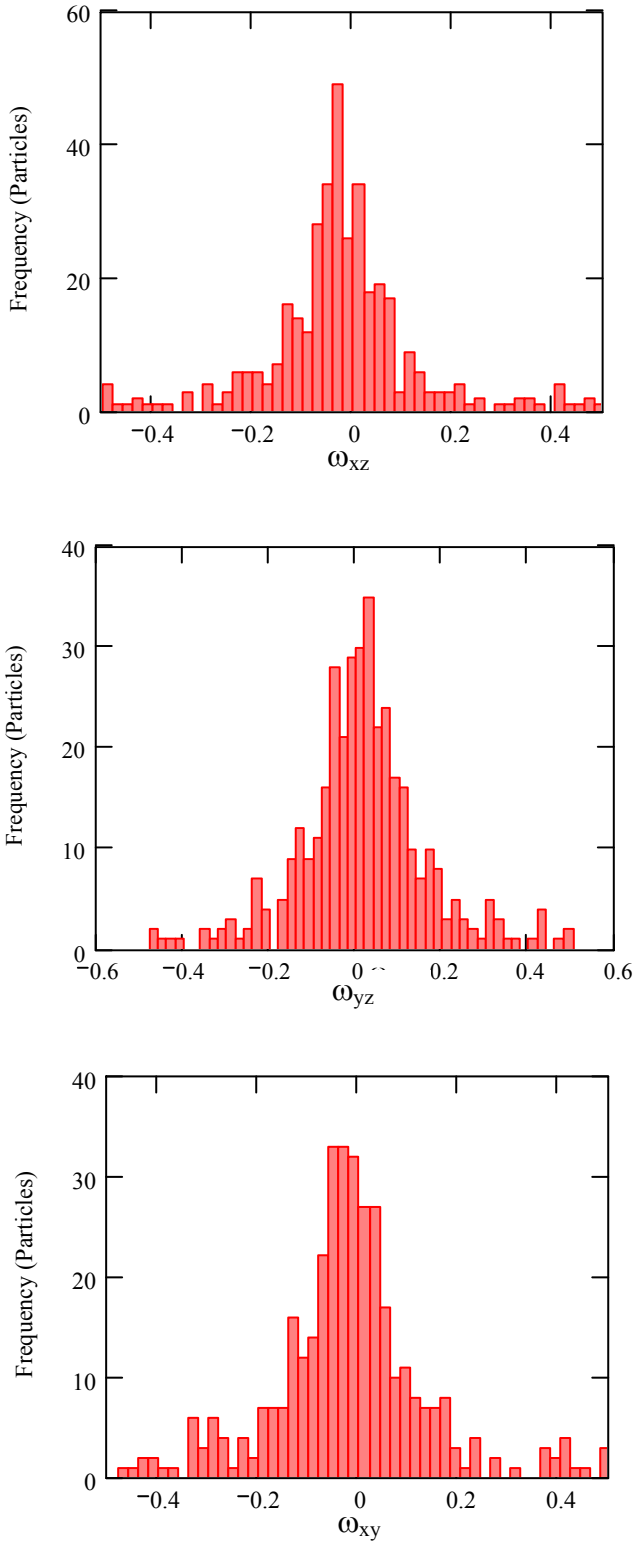

Figure B3: Rotation strains histograms at ε_z = -13.7%

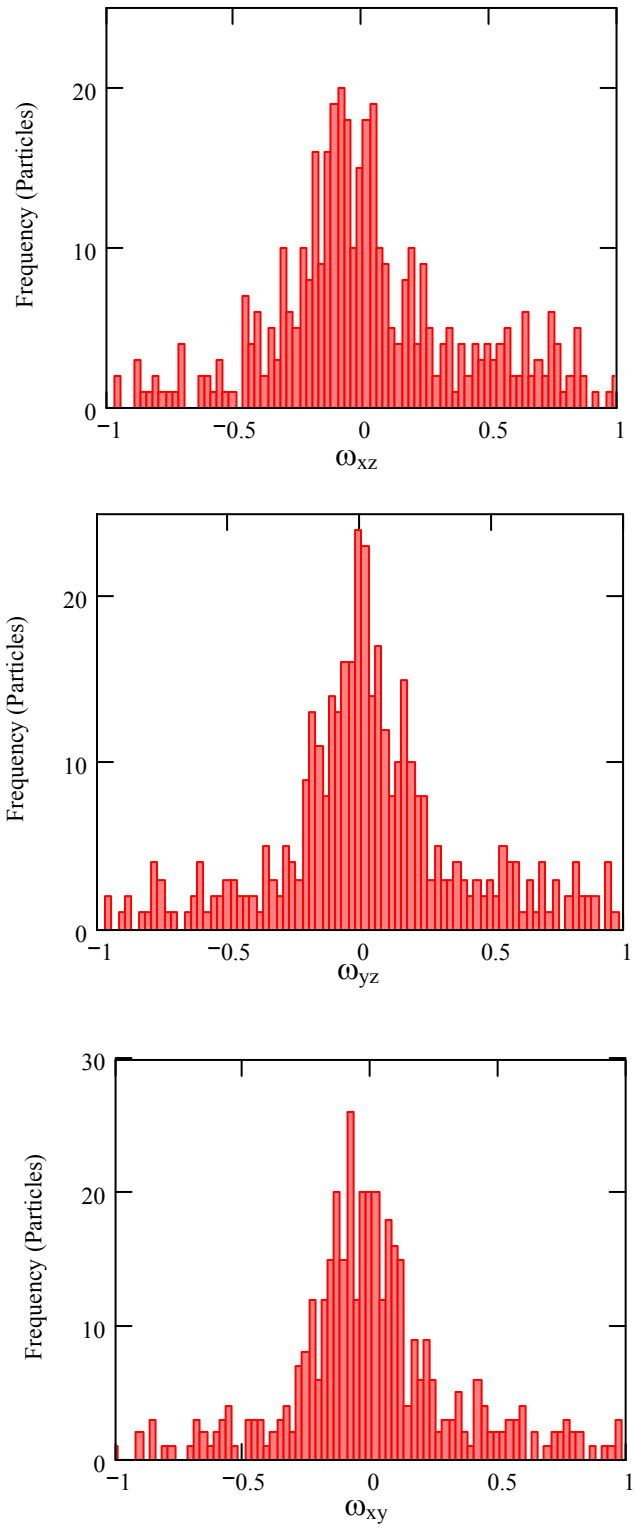

Figure B4: Rotation strains histograms at ε_z = -23.5%

VITA

Bashar Alramahi was born on September 7th, 1979, in Beirut, Lebanon. He studied high school at Al-Ittihad School in Amman, Jordan, and graduated in 1997. He received his bachelor's degree in civil engineering from Birzeit University, Ramallah, Palestine, in August, 2002. He came to the United States in January, 2003 to pursue a master's degree in geotechnical engineering at Louisiana State University, Baton Rouge, Louisiana. It is anticipated that he will fulfill the requirements for the master's degree in civil engineering in August, 2004.